Available online at www.sciencedirect.com

ScienceDirect

Geochimica et Cosmochimica Acta 238 (2018) 580–598

Geochimica et Cosmochimica Acta

www.elsevier.com/locate/gca

Experimentally determined effects of olivine crystallization and melt titanium content on iron isotopic fractionation in planetary basalts

Kelsey B. Prissel [a,*], Michael J. Krawczynski [a], Nicole X. Nie [b], Nicolas Dauphas [b], Hélène Couvy [a], Michael Y. Hu [c], E. Ercan Alp [c], Mathieu Roskosz [d]

[a] *McDonnell Center for the Space Sciences and Department of Earth and Planetary Sciences, Washington University in St. Louis, 1 Brookings Drive, St. Louis, MO 63123, United States*

[b] *Origins Laboratory, Department of the Geophysical Sciences and Enrico Fermi Institute, The University of Chicago, 5734 South Ellis Avenue, Chicago, IL 60637, United States*

[c] *Advanced Photon Source, Argonne National Laboratory, 9700 South Cass Avenue, Argonne, IL 60439, United States*

[d] *IMPMC, CNRS UMR 7590, Sorbonne Universités, Université Pierre et Marie Curie, IRD, Muséum National d'Histoire Naturelle, CP 52, 57 rue Cuvier, Paris F-75231, France*

Received 20 March 2018; accepted in revised form 22 July 2018; available online 31 July 2018

Abstract

Olivine is the most abundant mantle mineral at depths relevant to oceanic crust production through melting. It is also a liquidus phase for a wide range of mafic and ultramafic magma compositions. We have experimentally investigated the effects of olivine crystallization and melt composition on the fractionation of Fe isotopes in igneous systems. To test whether there is a melt compositional control on Fe isotopic fractionation, we have conducted nuclear resonant inelastic X-ray scattering (NRIXS) measurements on a suite of synthetic glasses ranging from 0.4 to 16.3 wt.% TiO_2. The resulting force constants are similar to those of the reduced ($fO_2 = IW$) terrestrial basalt, andesite, and dacite glasses reported by Dauphas et al. (2014), indicating that there is no measurable effect of titanium composition on Fe isotopic fractionation in the investigated compositional range. We have also conducted olivine crystallization experiments and analyzed the Fe isotopic composition of the experimental olivines and glasses using solution MC-ICPMS. Olivine and glass separates from a given experimental charge have the same iron isotopic composition within error. This result is robust in both the high-Ti glass (Apollo 14 black) and low-Ti glass (Apollo 14 VLT) compositions, and at the two oxygen fugacities investigated (IW−1, IW+2). Additionally, we have determined that Fe loss in reducing one-atmosphere gas-mixing experiments occurs not only as loss to the Re wire container, but also as evaporative loss, and each mechanism of experimental Fe loss has an associated Fe isotopic fractionation.

We apply our results to interpreting Fe isotopic variations in the lunar mare basalts and lunar dunite 72415-8. Our experimental results indicate that neither melt TiO_2 composition nor equilibrium olivine crystallization can explain the observed difference in the iron isotopic composition of the lunar mare basalts. Additionally, equilibrium iron isotopic fractionation between olivine and melt cannot account for the "light" iron isotopic composition of lunar dunite 72415-8, unless the melt from which it is crystallizing was already enriched in light iron isotopes. Our results support models of diffusive fractionation

* Corresponding author.
E-mail address: k.b.williams@wustl.edu (K.B. Prissel).

https://doi.org/10.1016/j.gca.2018.07.028

to explain the light iron isotopic compositions measured in olivine from a variety of rock types and reduced (fO_2 = IW−1 to IW+2) igneous environments (e.g., lunar dunite and basalts, terrestrial peridotites and basalts, martian shergottites).

Keywords: Iron isotopes; Olivine; Experimental petrology; NRIXS; Basalts

1. INTRODUCTION

Analytical developments over the past decade have revealed that igneous rocks and minerals display variations in the isotopic composition of non-traditional stable isotope systems (i.e., not C, H, N, O, S Teng et al., 2017, and references therein). The degree of mass-dependent fractionation between stable isotopes has been attributed to factors such as oxidation state, bonding environment, and volatility. While early studies focused on low-temperature stable isotopic fractionation, a growing number of studies have revealed measurable isotopic fractionations present in high temperature igneous systems (e.g., Beard and Johnson, 2004; Poitrasson et al., 2004; Weyer et al., 2005; Williams et al., 2005; Teng et al., 2008, and subsequent studies). Interpretations of these variations are often hampered by the paucity of equilibrium fractionation factors between coexisting phases, which limits quantitative modeling of the relevant igneous processes.

High-temperature stable isotopic fractionations have been used to elucidate planetary-scale processes, such as the formation of the Moon, as well as smaller scale processes, such as the differentiation of magma. In particular, high-precision studies of stable isotopes have resolved isotopic differences between terrestrial and lunar samples for certain elements (e.g., Wang and Jacobsen, 2016). However, for many isotopic systems, it is difficult to tell whether the Earth and Moon have different isotopic compositions because the processes of magmatic differentiation, including lunar magma ocean crystallization and later magma generation and crystallization, have imparted stable isotopic variations to lunar rocks that need to be understood and disentangled before a claim can be made regarding the bulk composition of the Earth or Moon. The increased precision of modern isotope analyses has resolved a "dichotomy" present between the bulk stable isotopic compositions of the low-Ti and high-Ti mare basalts on the Moon (Fig. 1). Specifically, this dichotomy has been observed for Fe (Wiesli et al., 2003; Poitrasson et al., 2004; Weyer et al., 2005; Craddock et al., 2010; Liu et al., 2010; Sossi and Moynier, 2017), with high-Ti mare basalts being isotopically "heavy" compared to low-Ti basalts ($\delta^{56}Fe_{high\text{-}Ti} > \delta^{56}Fe_{low\text{-}Ti}$). The dichotomy was also observed for Mg ($\delta^{26}Mg_{high\text{-}Ti} < \delta^{26}Mg_{low\text{-}Ti}$; Sedaghatpour et al., 2013), Li ($\delta^{7}Li_{high\text{-}Ti} > \delta^{7}Li_{low\text{-}Ti}$; Day et al., 2016), and Ti ($\delta^{49}Ti_{high\text{-}Ti} > \delta^{49}Ti_{low\text{-}Ti}$; Millet et al., 2016). Though the difference in stable isotopic compositions between the high- and low-Ti basalts is well documented analytically, the petrologic processes responsible for the lunar isotopic dichotomy remain elusive.

Despite increasing evidence for high-temperature isotopic fractionation in igneous rocks (e.g., Dauphas and Rouxel, 2006; Dauphas et al., 2017), there is a paucity of experimental studies of isotopic fractionation during magmatic differentiation of mafic compositions. The iron isotopic compositions of igneous rocks have been extensively studied, and the documented isotopic variations in igneous rocks are caused by a combination of partial melting (e.g., Williams et al., 2005; Weyer and Ionov, 2007; Dauphas et al., 2009a, 2014; Williams and Bizimis, 2014), equilibrium and fractional crystallization (e.g., Teng et al., 2008; Dauphas et al., 2014; Roskosz et al., 2015), and diffusive fractionation (e.g., Dauphas and Rouxel, 2006; Sio et al., 2013; Oeser et al., 2015; Sio and Dauphas, 2016; Collinet et al., 2017). Experimental studies of equilibrium Fe isotope partitioning at high temperature have investigated metal-silicate systems, fayalite-magnetite fractionation, as well as Fe isotopic fractionation between evolved rhyolitic compositions and sulfides (e.g., Schuessler et al., 2007; Shahar et al., 2008; Poitrasson et al., 2009). Additionally, Dauphas et al. (2014) investigated the Fe bonding structure in a suite of terrestrial volcanic glass compositions ranging from basalt to rhyolite, concluding that Fe isotopic composition is influenced by the redox state of iron and the silica content of the melt.

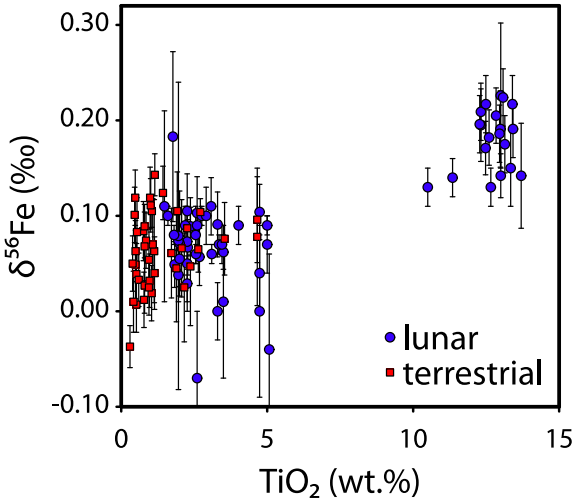

Fig. 1. Iron isotopic compositions plotted as a function of TiO_2. Red points represent terrestrial basalts and andesites, and blue points represent lunar basalts. The terrestrial suite is similar in Fe isotopic composition to the low-Ti basalts, however high-Ti basalts have greater $\delta^{56}Fe$ values. The observed fractionation between low- and high-Ti lunar mare basalts appears to be bi-modal, although it is uncertain if this modality is due to sampling bias, as basalts with intermediate Ti concentrations have not been frequently measured. Compositions and isotope measurement errors (95% confidence interval) are from (Wiesli et al., 2003; Poitrasson et al., 2004; Weyer et al., 2005; Teng et al., 2008; Dauphas et al., 2009b; Schuessler et al., 2009; Craddock et al., 2010; Liu et al., 2010; Wang et al., 2015; Sossi and Moynier, 2017).

Evidence for mineralogical, compositional, and redox controls on Fe isotope partitioning in igneous rocks highlights the importance of experimentally quantifying mineral-melt fractionations for major rock-forming minerals. Olivine is a ubiquitous mineral on rocky, differentiated planetary bodies. Even a small (<0.1‰) olivine-melt Fe isotopic fractionation could significantly fractionate the Fe isotopes in mantle reservoirs during planetary differentiation; for example, an olivine-melt fractionation $\delta^{56}Fe_{olivine} - \delta^{56}Fe_{melt} = -0.05‰$ would increase the $\delta^{56}Fe$ of a magma ocean by 0.1‰ after 50% fractional crystallization of olivine. The measured iron isotopic compositions of olivine separates are often used to interpret olivine-melt fractionations (e.g., Williams et al., 2005; Wang et al., 2015). Yet, naturally occurring minerals have complex crystallization-cooling histories, and inferring an equilibrium fractionation factor from such measurements is fraught with difficulties. The use of natural samples to determine olivine-melt equilibrium iron isotopic fractionations is complicated by diffusion-driven, kinetic iron isotopic fractionations (e.g., Teng et al., 2008, 2011; Sio et al., 2013). In terrestrial igneous rocks, both Fe^{2+} and Fe^{3+} coexist, which can cause equilibrium isotopic fractionation between melt and olivine (i.e., Teng et al., 2008; Dauphas et al., 2009a). Redox-driven fractionation on Earth may obscure the existence of equilibrium iron isotopic fractionation between olivine and Fe^{2+} in silicate melt. On the other hand, large Fe isotopic fractionations exist among lunar basalts in an environment relatively free of Fe^{3+}. The absence of Fe^{3+} on the Moon supports mechanisms of mineral fractionation, melt composition, and/or diffusive re-equilibration as cause for the observed iron isotopic variation between the low- and high-Ti mare basalts. The iron isotopic fractionations associated with these equilibrium and kinetic processes need to be well-characterized in order to distinguish the effects of each process on the resulting iron isotopic compositions of igneous rocks.

To investigate the effects of melt composition and olivine crystallization on Fe isotopic fractionation, we have experimentally determined the olivine-melt equilibrium partitioning of Fe isotopes for a compositional suite of synthetic lunar volcanic glasses. We have implemented a dual approach, combining independent techniques (MC-ICPMS and NRIXS) for determining equilibrium Fe isotopic fractionations between high temperature phases. In focusing our experimental study on compositions and oxygen fugacities relevant for lunar differentiation, we investigated Fe isotopic fractionation in the case where Fe^{3+} is of negligible abundance. Furthermore, in experimentally examining the Fe isotope dichotomy between high-Ti and low-Ti lunar mare basalts, we have examined whether the bulk titanium content of a melt exhibits a compositional control on the resulting Fe isotope signature of the basalt.

2. METHODS

We have investigated the equilibrium fractionation of Fe isotopes between olivine and melt using two independent techniques. To determine the melt compositional control on Fe isotopic fractionation between lunar melts and olivine, we have conducted nuclear resonant inelastic X-ray scattering (NRIXS) measurements on a suite of synthetic glasses ranging from 0.4 to 16.3 wt.% TiO_2. To evaluate the magnitude of iron isotopic fractionation at equilibrium between olivine and melt, we have conducted olivine crystallization experiments and analyzed the Fe isotopic composition of the experimental olivines and glasses using solution MC-ICPMS. Direct olivine crystallization experiments were conducted using two bulk compositions: a synthetic glass similar to Apollo 14 VLT (very low Ti), and a synthetic Apollo 14 black glass (Table 1). Both of these compositions have olivine as a liquidus phase at one atmosphere pressure.

In comparing the results of both the NRIXS and direct crystallization experimental methods, we have determined the effect of equilibrium olivine crystallization and melt titanium content on Fe isotopic fractionation during high-temperature igneous processes. Additionally, the reducing experimental run conditions minimize Fe^{3+} content in the olivine and glass, making our results directly applicable to lunar oxygen fugacity conditions (IW−2 to IW+1; Sato, 1973).

2.1. Starting materials

For the NRIXS measurements, synthetic lunar ultramafic volcanic glass compositions were prepared from oxide powders to match the Apollo 16 green (0.39 wt.% TiO_2), Apollo 14 yellow (4.58 wt.% TiO_2), Apollo 17 orange (8.63 wt.% TiO_2), and Apollo 14 black (16.4 wt.% TiO_2) glass compositions given in Delano (1986) (Table 1). These glasses were chosen to span the range of TiO_2 content in the picritic lunar glass suite. Sodium and potassium were added to the mixtures as carbonates (Na_2CO_3, K_2CO_3), calcium was added as $CaSiO_3$, and all other components were added as single element oxides. In order to perform the NRIXS measurements, which are only sensitive to the Mössbauer isotope ^{57}Fe, ^{57}Fe-enriched Fe_2O_3 powder (96.64% ^{57}Fe, Cambridge Isotopes) was used. Oxides were mixed by hand under isopropanol in an agate mortar and pestle for 20 minutes.

Table 1
Reference lunar volcanic glass compositions from Delano (1986).

Composition	SiO_2	TiO_2	Al_2O_3	Cr_2O_3	FeO	MnO	MgO	CaO	Na_2O	K_2O
Apollo 14 VLT	46.00	0.55	9.30	0.58	18.20	0.21	15.90	9.24	0.11	0.07
Apollo 16 Green	43.90	0.39	7.83	0.39	21.90	0.24	16.90	8.44	–	–
Apollo 14 Yellow	40.80	4.58	6.16	0.41	24.70	0.30	14.80	7.74	0.42	0.10
Apollo 17 Orange	39.40	8.63	6.21	0.67	22.20	0.28	14.70	7.53	0.41	0.04
Apollo 14 Black	34.00	16.40	4.60	0.92	24.50	0.31	13.30	6.90	0.23	0.16

For the olivine crystallization experiments, the starting materials were prepared to be similar in composition to the synthetic Apollo 14 VLT (green) and Apollo 14 black glasses in Delano (1986) (Table 1). Calcium was added as $CaCO_3$ for the green glass, and $CaTiO_3$ for the black glass. Compositions used for the olivine crystallization experiments contained natural Fe isotope abundances and were mixed without the addition of Cr, Na, or K. Oxides, silicates, carbonates, and titanates were mixed under isopropanol in a silicon-nitride ball mill for 3 h. Polyvinyl alcohol was added as a binding agent to the starting material mixtures for both the NRIXS and olivine crystallization techniques. Once dry, 75 mg aliquots of each mixture were pressed into cylindrical pellets of 4 mm diameter and 2 mm height in preparation to be melted in the gas-mixing furnace. Great care was exercised to ensure that no cross-contamination took place between the experiments involving enrichment in ^{57}Fe and those with natural Fe isotopic abundances. However, select experiments did exhibit slight enrichments in ^{57}Fe (as detailed in the Supplementary Material). By focusing on $\delta^{56}Fe$, we minimize any potential effects of ^{57}Fe contamination.

2.2. Experimental Methods

Lunar volcanic glass syntheses and olivine crystallization experiments were conducted in vertical gas-mixing furnaces at Washington University in St. Louis. Sample pellets were fused to rhenium loops and hung by a Pt wire thread in the furnace hot spot for the run duration. Experimental samples were then quenched rapidly by melting the Pt hanging wire and dropping the sample from within the furnace into a beaker of deionized water. The ^{57}Fe-doped glass syntheses were conducted for approximately 3 h at 1400 °C and an oxygen fugacity corresponding to the iron-wüstite buffer (Table 2). Olivine crystallization experiments were conducted at fO_2 values of IW−1 and IW+2 for durations of 6 h, 1 day, and 4 days (Table 2). The temperatures for the olivine crystallization experiments ranged from 1262 to 1269 °C, with ±1 °C variation during a given experimental run (Table 2). These temperatures were optimal for producing low modal abundances (10–20 wt.%) of large olivine crystals.

All experimental run products were synthesized at oxygen fugacities that bracket the oxygen conditions inferred for the Moon. These reducing conditions minimize the presence of Fe^{3+}, which has been demonstrated to affect Fe isotope partitioning (e.g., Dauphas et al., 2014). A controlled flow of H_2 and CO_2 gases buffered the oxygen fugacity throughout each experiment. The fugacity was monitored with a Ca-doped zirconia oxygen probe using air as the reference gas. The fO_2 was found to vary between 0.01 and 0.15 log units (1σ standard deviation) during a given experiment (Table 2).

Long experimental run durations aided in crystal growth, allowing for clean mechanical separation of olivine grains for MC-ICPMS work. Olivine grains from our four-day experiments exhibited a range in grain diameter from 20 to 100 μm, compared to the 5 to 50 μm grain diameter range for the one-day experiments (Fig. 2). However, Fe loss from an experimental charge increases with increased run duration (Table 2, Fig. 3a). Thus, a four-day run duration was deemed optimal for the olivine crystallization experiments needed to minimize Fe loss from the experiment, while providing experimental olivines large enough to hand-separate for MC-ICPMS measurements. To ensure that clean olivine and glass could be retrieved for MC-ICPMS work, olivine and glass were separated from the four-day experiments. Quantitative analysis of the Fe loss in these experiments is presented in Section 4.1.

2.3. Approach to equilibrium

The experimentally produced olivines are compositionally homogenous and do not exhibit compositional zoning within the grains (Fig. 2), and electron microprobe compositional analyses show low standard deviations amongst all analyzed grains in a given sample (Table 3). Mineral-liquid Fe-Mg exchange coefficients ($K_D^{Fe\text{-}Mg}$, Table 2) for our olivine-bearing experiments are a function of melt Ti content (0.32–0.34 for 0.06 wt.% TiO_2; 0.23–0.26 for 18 wt.% TiO_2) and are consistent with the results of Krawczynski and Grove (2012). In addition, a time series of experiments was conducted for each experimental starting composition (Apollo 14 VLT green glass, Apollo 14 black glass) at each experimental oxygen fugacity (IW−1, IW+2) in order to evaluate the effect of experimental Fe loss on the olivine-melt equilibrium. Experimental iron loss increases with increased run duration and decreased oxygen fugacity (Table 2). Thus, the lowest oxygen fugacity ($fO_2 = IW-1$) experiments experienced significant (up to 18%) Fe loss during the four-day experiments (see discussion in Section 4.1). Despite the increased Fe loss, the mineral-liquid Fe-Mg exchange coefficients for the four-day experiments are the same as those calculated for the shorter duration experiments (Table 2), indicating that olivine-melt equilibrium was maintained.

2.4. Analytical methods

2.4.1. Electron microprobe analysis

Experimental run products were analyzed for major element abundances using the JEOL JXA-8200 electron microprobe at Washington University in St. Louis. Standardization was performed with a beam diameter of 20 μm on natural and synthetic glass and mineral samples. We used the mean atomic number (MAN) method (Donovan et al., 2016) for wavelength dispersive spectrometer background correction and measured the following elements: Si, Al, Ti, Cr, Fe, Mn, Mg, Ca, Na, K. Each quantitative analysis used a 15 kV accelerating potential and 25nA beam current. Glass compositions were analyzed with a 20 μm beam diameter, and olivine compositions were analyzed with a focused beam (~1 μm diameter). Each compositional data point was reduced using *Probe for EPMA* software. Averages of the analyzed glass and olivine compositions are reported in Table 3. Only analyses with totals 98.5–101.5 weight percent (wt.%) are included in the reported averages (with the exception of experiment J021, for which the analytical totals were on average 96.75 wt.%

Table 2
Experimental run conditions and products.

Experiment	Composition	Mix	Time (hr)	T (°C)	$\log_{10} fO_2$	Δ IW	Phases (calculated mode)	Olivine K_D	% Fe loss/gain
NRIXS ^{57}Fe-doped glasses									
J020	Apollo 16 Green	#14	2.9	1400	−9.7	0.0	Glass (100)	–	−3.5
J021	Apollo 14 Yellow	#15	3.6	1399	−9.8	−0.1	Glass (100)	–	−6.7
J022	Apollo 14 Black	#17	2.6	1400	−9.8	−0.1	Glass (100)	–	−2.1
J023	Apollo 17 Orange	#16	2.8	1400	−9.7	0.0	Glass (100)	–	−2.4
Green IW−1 Series									
J017	Apollo 14 VLT	#10	5.9	1266	−12.2	−1.1	Glass (81) + ol (19)	0.32	−4.6
J019	Apollo 14 VLT	#10	23.4	1266	−12.2	−1.1	Glass (82) + ol (18)	0.34	−5.4
J040	Apollo 14 VLT	#29	96.2	1262	−12.1	−1.0	Glass (83) + ol (17)	0.34	−17.9
H056	Apollo 14 VLT	#29	96.4	1266	−12.2	−1.0	–	–	–
Black IW−1 Series									
H042	Apollo 14 Black	#11	6.0	1266	−12.1	−1.0	Glass (90) + ol (10)	0.24	−3.4
H025	Apollo 14 Black	#5	22.4	1265	−11.1	0.1	Glass (90) + ol (10)	0.24	−5.7
H057	Apollo 14 Black	#28	92.9	1263	−12.1	−1.0	Glass (92) + ol (8)	0.26	−17.9
H043	Apollo 14 Black	#11	96.0	1266	−12.2	−1.0	–	–	–
H055	Apollo 14 Black	#28	94.1	1267	−12.1	−1.0	–	–	–
Green IW+2 series									
J009	Apollo 14 VLT	#10	5.5	1269	−9.2	1.9	Glass (83) + ol (17)	0.32	0.3
H031	Apollo 14 VLT	#10	24.1	1266	−9.2	2.0	Glass (83) + ol (17)	0.32	−1.9
J007	Apollo 14 VLT	#10	96.0	1268	−9.2	1.9	Glass (84) + ol (16)	0.32	−8.4
H030	Apollo 14 VLT	#10	96.0	1265	−9.1	2.0	–	–	–
Black IW+2 series									
H039	Apollo 14 Black	#11	6.3	1265	−9.2	2.0	Glass (92) + ol (8)	0.23	−4.2
H038	Apollo 14 Black	#11	24.2	1266	−9.1	2.0	Glass (91) + ol (9)	0.23	−6.0
H037	Apollo 14 Black	#11	96.3	1266	−9.1	2.0	Glass (91) + ol (9)	0.24	−8.8
J012	Apollo 14 Black	#11	96.3	1266	−9.1	2.0	–	–	–

"K_D" represents the olivine-melt Fe-Mg exchange coefficient calculated by $(X^{ol}_{Fe} * X^{melt}_{Mg})/(X^{melt}_{Fe} * X^{ol}_{Mg})$.
"% Fe loss/gain" is estimated using the FeO content of the starting composition and the FeO content of the sample (calculated from the phase compositions and modal abundances).
For mixes #5, #10, and #11, FeO was added as a mixture of Fe metal sponge and Fe_2O_3 oxide powder. All other mixes were prepared with only Fe_2O_3.

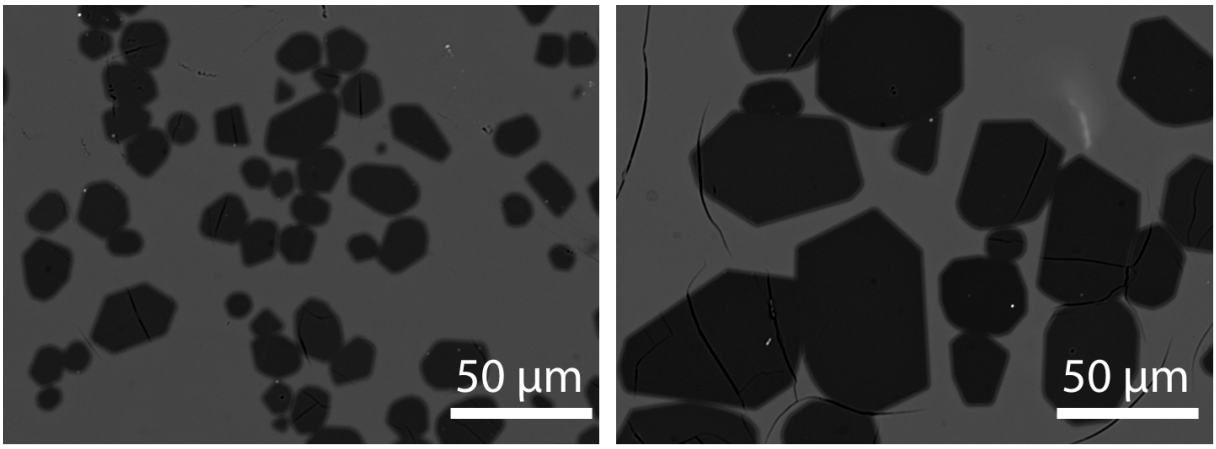

Fig. 2. Back scattered electron image of two olivine crystallization experiments. Both experiments were conducted at $fO_2 = IW+2$. Experiment durations were 1 day (left) and 4 days (right). Experimental olivine crystals (dark gray) in the 4-day experiment (~50 µm diameter) are larger than those grown in the 1-day experiment (~20 µm). Additionally, the olivine grains are compositionally homogenous, i.e., there is no visible Fe zoning within the grains at the ± 0.5 wt.% FeO level.

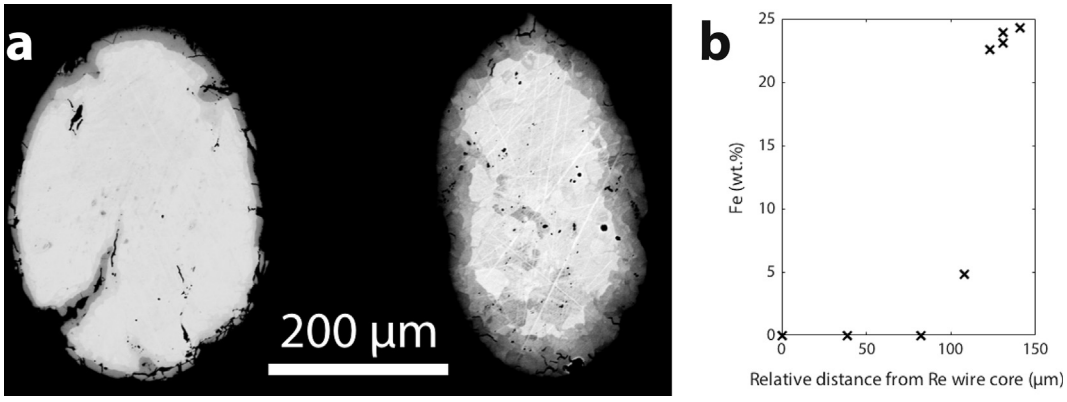

Fig. 3. (a) Back scattered electron image of two Re wires. The wires were mounted in epoxy post-experiment and polished to create a measureable cross section. Both wires were used in experiments conducted at $fO_2 = IW-1$. Experiment durations were 6 h (left) and 4 days (right). Experimental Fe loss to the Re wire increases with time, producing a thicker Fe-enriched layer (dark gray) while the core of the Re wire remains Fe-free (light gray). (b) Electron microprobe core-to-rim Fe (wt.%) profile in a Re wire from a 4-day experiment conducted at $fO_2 = IW-1$.

likely due to incomplete degassing of the carbonates in the starting material). Olivine analyses were filtered to include only those with olivine stoichiometry (cation total between 2.98 and 3.02 for 4 oxygen atoms). The same calibration was used for the compositional analysis of the experimental wires, with pure Re, Fe, and Pt metal samples added as analytical standards. The Re experiment wires were analyzed from core to rim with a 2 µm beam diameter.

2.4.2. Nuclear Resonant Inelastic X-ray Scattering Spectroscopy (NRIXS) methods

Nuclear resonant inelastic X-ray scattering spectroscopy (NRIXS) was used to probe the excitation modes of iron atoms and derive quantities needed to calculate equilibrium fractionation factors. From the phonon excitation probability function, $S(E)$, or the partial phonon density of states, $g(E)$, (itself derived from S), the force constant for the iron sublattice can be extracted (e.g., Dauphas et al., 2012; Dauphas et al., 2014; Liu et al., 2017) (also see Polyakov et al., 2007 for a different approach based on the kinetic energy). Assuming that the bonds are harmonic and given the high temperatures involved in magmatic processes, the reduced partition function ratio, or β-factor is calculated as a function of temperature from the mean force constant of the iron bonds, $\langle F \rangle$ in N/m (the higher order terms needed to calculate iron β-factors at low temperature are given in Table 4):

$$1000 \ln \beta = 2904 \frac{\langle F \rangle}{T^2} \quad (1)$$

At a given temperature, the equilibrium stable isotopic fractionation factor (e.g., $\alpha_{\text{mineral-melt}}$) between two phases is related to the β-factor and Fe isotopic composition (δ^{56}Fe) for each phase through:

Table 3
Electron microprobe analyses of experimental run products in oxide weight percent.

Experiment	Phase	n[1]	SiO_2	s.d.	TiO_2	s.d.	Al_2O_3	s.d.	Cr_2O_3	s.d.	FeO	s.d.	MnO	s.d.	MgO	s.d.	CaO	s.d.	Na_2O	s.d.	K_2O	s.d.	Total
NRIXS ^{57}Fe-doped glasses																							
J020	glass	17	44.69	0.18	0.40	0.02	7.95	0.04	0.41	0.01	21.02	0.12	0.19	0.02	16.19	0.07	8.18	0.04	0.04	0.01	0.011	0.003	99.08
J021	glass	15	41.17	0.18	4.39	0.04	5.55	0.06	0.57	0.01	23.02	0.13	0.28	0.02	14.21	0.08	7.35	0.04	0.18	0.01	0.039	0.006	96.75
J022	glass	13	33.95	0.12	16.27	0.11	4.65	0.03	0.77	0.02	23.71	0.08	0.16	0.01	12.85	0.09	6.61	0.03	0.08	0.01	0.019	0.004	99.07
J023	glass	13	40.17	0.13	8.69	0.07	6.00	0.03	0.26	0.01	21.67	0.15	0.36	0.02	14.42	0.07	7.31	0.05	0.16	0.01	0.021	0.005	99.05
Green IW−1 Series																							
J017	glass	11	47.85	0.18	0.64	0.03	11.51	0.33			16.80	0.27	0.16	0.02	10.51	0.27	11.37	0.38					98.83
	olivine	17	38.98	0.34	b.d.		0.05	0.05			20.36	0.86	0.15	0.02	40.05	0.76	0.33	0.07					99.91
J019	glass	14	48.08	0.18	0.62	0.02	11.55	0.05			16.55	0.11	0.15	0.01	10.65	0.10	11.39	0.04					98.99
	olivine	20	38.73	0.67	b.d.		0.31	1.18			20.80	0.15	0.14	0.02	39.84	0.55	0.35	0.05					100.17
J040	glass	19	49.28	0.21	0.67	0.02	11.46	0.06			14.37	0.13	0.21	0.02	11.27	0.04	11.61	0.04					98.87
	olivine	16	39.47	0.24	b.d.		0.03	0.01			18.13	0.21	0.21	0.02	41.99	0.31	0.29	0.01					100.11
Black IW−1 Series																							
H042	glass	16	33.43	0.24	18.13	0.20	5.18	0.04			23.86	0.21	0.27	0.02	10.36	0.09	7.50	0.03					98.74
	olivine	19	38.24	0.44	0.65	0.78	0.05	0.05			21.59	0.38	0.19	0.02	39.07	0.48	0.21	0.03					100.00
H025	glass	18	34.08	0.35	18.08	0.16	5.29	0.07			23.32	0.15	0.28	0.02	10.64	0.20	7.54	0.08					99.22
	olivine	7	39.14	0.24	0.16	0.04	b.d.				21.28	0.09	0.20	0.02	40.01	0.37	0.17	0.02					100.96
H057	glass	13	35.65	0.11	18.35	0.08	5.40	0.05			20.19	0.13	0.35	0.03	11.34	0.06	7.59	0.04					98.86
	olivine	24	39.14	0.16	0.21	0.05	0.02	0.01			18.90	0.18	0.25	0.02	41.58	0.21	0.15	0.01					100.24
Green IW+2 series																							
J009	glass	15	47.40	0.40	0.64	0.02	11.20	0.20			17.86	0.22	0.20	0.02	10.81	0.20	11.09	0.07					99.20
	olivine	13	38.74	0.48	b.d.		0.06	0.08			20.86	0.41	0.19	0.02	39.77	0.60	0.39	0.02					100.01
H031	glass	18	47.67	0.29	0.65	0.02	11.44	0.09			17.46	0.14	0.19	0.02	10.88	0.10	11.06	0.05					99.35
	olivine	7	39.04	0.19	b.d.		0.04	0.01			20.53	0.17	0.19	0.02	39.98	0.25	0.36	0.02					100.13
J007	glass	19	48.64	0.24	0.65	0.02	11.38	0.14			16.27	0.20	0.20	0.01	11.23	0.15	11.19	0.08					99.56
	olivine	10	39.54	0.08	b.d.		0.04	0.01			19.47	0.46	0.19	0.01	41.43	0.40	0.33	0.02					101.00
Black IW+2 series																							
H039	glass	13	33.72	0.26	17.64	0.07	5.14	0.03			23.73	0.13	0.31	0.02	10.84	0.09	7.45	0.04					98.83
	olivine	12	38.80	0.26	0.30	0.16	0.05	0.06			20.67	0.25	0.24	0.02	40.79	0.52	0.23	0.05					101.08
H038	glass	11	33.83	0.12	17.93	0.10	5.17	0.03			23.27	0.16	0.31	0.02	10.75	0.06	7.56	0.02					98.82
	olivine	13	38.90	0.27	0.15	0.03	0.03	0.01			20.62	0.17	0.24	0.03	40.93	0.17	0.20	0.01					101.07
H037	glass	13	34.18	0.13	18.02	0.07	5.23	0.03			22.54	0.10	0.32	0.02	10.93	0.04	7.59	0.04					98.82
	olivine	15	38.57	0.45	0.12	0.02	0.02	0.01			20.31	0.17	0.25	0.02	40.93	0.43	0.20	0.01					100.40

Cr_2O_3, Na_2O, and K_2O were not measured in the olivine crystallization experiments.
"b.d." indicates that the measured composition was below detection limit.
[1] Compositions are reported as an average of "n" analyses. Oxide measurements are reported with 1σ standard deviation in the adjacent "s.d." column.

Table 4
Mean force constants for synthetic lunar volcanic glass suite.

Sample	⟨F⟩ (N/m)	1000ln β = A/T^2 + B/T^4 + C/T^6 (T in K)		
		A (×10^5)	B (×10^9)	C (×10^{13})
Apollo 16 Green (J020)	189 ± 9	5.36 ± 0.26	−4.29 ± 0.68	12.34 ± 3.60
Apollo 14 Yellow (J021)	195 ± 12	5.55 ± 0.34	−4.87 ± 0.99	16.20 ± 5.57
Apollo 17 Orange (J023)	203 ± 11	5.79 ± 0.32	−4.90 ± 0.79	13.24 ± 3.81
Apollo 14 Black (J022)	191 ± 11	5.45 ± 0.31	−4.35 ± 0.74	11.48 ± 3.45
Fo_{82} Olivine[1]	197 ± 10	5.61 ± 0.28	−2.59 ± 0.44	3.04 ± 1.14

[1] Olivine force constant data from Dauphas et al. (2014).

$$1000\ \ln\ \alpha_{mineral-melt} = \delta^{56}Fe_{mineral} - \delta^{56}Fe_{melt} = 1000\ \ln\ \beta_{mineral} - 1000\ \ln\ \beta_{melt} \quad (2)$$

Using the measured force constants for synthetic lunar glasses and olivine (Dauphas et al., 2014), the equilibrium fractionation factor between olivine and melt can be theoretically determined using Eq. (2), assuming that the iron force constant in the glass is not significantly different from that of a melt of the same composition.

2.4.3. Multicollector-Inductively Coupled Plasma Mass Spectrometry (MC-ICPMS) methods

The quenched experimental samples were crushed, and then individual phases were hand separated for Fe isotopic analysis with a Thermo Scientific Neptune MC-ICPMS in the Origins Lab at the University of Chicago. The instrument was upgraded in the course of its life by addition of an OnToolBooster Jet pump, bringing it to specifications on par with the Neptune Plus model. Olivine grains were hand-picked from the experimental samples under an optical microscope using cross-polarized light to distinguish the birefringent olivines from the isotropic glass. Separated olivine grains ranged between 30 and 100 μm in diameter and contained minor amounts of glass, present as thin layers on the edge of the grains. Glass separates were approximately 50–150 μm in diameter, and the transparency of the glass allowed for separation of glass pieces that were free of olivine grains.

Olivine and glass separates were then dissolved for MC-ICPMS analysis. The starting material powders, used experiment wires, and "total samples" (experimental sample left after minor glass and olivine separate removal) were also dissolved and measured to aid in interpretation of the measured isotopic compositions (see Section 4.1). Following the routine sample dissolution protocol of the Origins Lab (e.g., Dauphas et al., 2009b; Craddock and Dauphas, 2011), we digested 10–40 mg of each sample through hot-plate acid dissolution with mixtures of concentrated HF-HNO_3-$HClO_4$ and HCl-HNO_3-$HClO_4$. An additional dissolution step using aqua regia (3:1 ratio of HCl-HNO_3) was used for the starting material powders, Re wires, and "total samples". This step was repeated three times to ensure all of the Fe had been dissolved from the samples. However, a white residue (rich in TiO_2 and Al_2O_3), remained after two weeks of dissolution for the starting material powders and "total samples". Analysis of the white residues by electron dispersive spectroscopy confirmed that there was no Fe present, indicating that the dissolution effectively removed all Fe from the samples despite the remaining white residue. After the heated dissolution steps, each sample was dried out (the samples with visible residues were centrifugated and the supernatants were used), then dissolved in 6 M HCl in preparation for Fe column chemistry.

The sample solutions were purified for Fe through column chemistry following the routine methods of the Origins Lab at the University of Chicago (e.g., Dauphas et al., 2004, 2009b; Dauphas and Rouxel, 2006). The iron isotopic compositions of the sample solutions were measured using the standard-bracketing method of Dauphas et al. (2009b), and are reported as δ^{56}Fe relative to IRMM-524, whose isotopic composition is identical to IRMM-014 (Craddock and Dauphas, 2011).

3. RESULTS

Here we report experimentally determined mean force constants of iron bonds in synthetic glass samples and iron isotopic compositions of synthetic olivine and glass separates. Iron isotopic fractionation factors determined from the force constants and iron isotopic compositions demonstrate an absence of resolvable iron isotopic fractionation during olivine crystallization in reducing (fO_2 = IW−1 to IW+2) conditions.

3.1. NRIXS Results

The force constants calculated from NRIXS spectra on our synthetic lunar glasses show that within error, the lunar glasses have the same force constant, averaging to a value of 195 ± 22 N/m (Table 4). This similarity in force constants over the 0.4–16.3 wt.% TiO_2 range of our synthetic glasses suggests that Fe isotopic fractionation is not a function of melt Ti content (Fig. 4). Further, the mean force constants of our synthetic suite of lunar glasses are similar to the force constants generated for reduced (fO_2 = IW) terrestrial basalts (197 ± 8 N/m) in Dauphas et al. (2014). The force constants from the synthetic lunar glasses are also similar to the previously determined iron force constant for olivine (Fo_{86}, Fe^{3+} absent) of 197 ± 10 N/m (Dauphas et al., 2014).

3.2. Olivine crystallization experiments

The measured Fe isotopic compositions of the experimental glass and olivine separates indicate that there is no

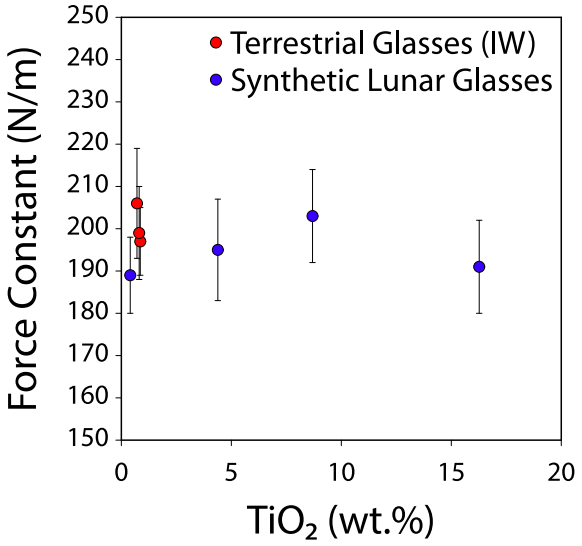

Fig. 4. Force constants from a suite of melt compositions plotted as a function of TiO_2 content. Red points represent the reduced ($fO_2 = IW$) terrestrial basalt, andesite, and dacite glasses from Dauphas et al. (2014), and blue points represent the synthetic lunar volcanic glass compositions measured in this work. There is no correlation between force constants and TiO_2 content within the investigated 0.4–16.3 wt.% TiO_2 compositional range.

measurable fractionation between olivine and glass (Table 5). The isotopic difference between the starting material, experiment wire, and olivine and glass separates can be explained by the fractionation of Fe isotopes during experimental Fe loss to the Re wire and through evaporation (Section 4.1). The iron isotopic composition of the starting material powders (Table 5) is controlled by both the iron isotopic composition of Fe_2O_3 (used in all starting compositions) and Fe metal sponge (used only in starting compositions #010 and #011) (Appendix Table 1). To further illustrate the isotopic relationship among all experimental parts, the measured Fe isotopic compositions have been plotted in Fig. 5. For each experiment, the olivine Fe isotopic composition is indistinguishable from that of the glass. The measured compositions thus indicate that olivine does not significantly fractionate iron isotopes when crystallizing from lunar melt compositions at lunar-like fO_2.

4. DISCUSSION

4.1. Quantitative analysis of experiment iron loss

The four-day olivine crystallization experiments experienced up to 18% total Fe loss (Table 2). We estimated the amount of total Fe loss using a mass balance of the measured phase compositions and the bulk starting composition of the experiment (Krawczynski and Olive, 2011). A rhenium wire was used in all of the experiments to minimize the diffusive Fe loss to the metal loop at reduced oxygen fugacities (Borisov and Jones, 1999). The experimental runs at $fO_2 = IW+2$ experienced less Fe loss than those at $fO_2 = IW-1$ (9% vs. 18% Fe loss, Table 2). The total amount of iron lost from our experiments under reducing conditions is consistent with the estimated loss in experiments ran at similar conditions by Borisov and Jones (1999). Electron microprobe analyses of the Re wires after completion of the experiments (Fig. 3b, Appendix Table 2) yield Fe concentrations within the range of those measured in Re wires from Borisov and Jones (1999). The Re wire is always enriched in the light isotopes of iron, which is consistent with the fact that transport through the wire is diffusive, and light isotopes of iron diffuse faster than heavier ones (Mullen, 1961; Roskosz et al., 2006; Dauphas, 2007; Richter et al., 2009; Van Orman and Krawczynski, 2015). However, the Fe mass balance between the wire and sample cannot account for all of the sample Fe loss.

To account for the effect of Fe loss on the measured Fe isotopic compositions of the samples, we measured the Fe isotopic compositions of the bulk starting material, experiment wire, and the sample material remaining after olivine and glass separates were removed (Table 5). Owing to their similar Fe isotopic compositions, removal of minor olivine and glass fractions from the sample did not change the bulk isotopic composition of the remaining sample material (unseparated glass and olivine, hereafter referred to as "total sample"). For each of the olivine crystallization experiments, the isotopic compositions ($\delta^{56}Fe$) of the total sample were higher than that for the bulk starting material. Open system behavior of Fe and isotopic fractionation between the bulk starting material and the total sample can be explained by Fe loss to the Re wire and evaporative Fe loss in the gas-mixing furnace. Using the measured iron isotopic compositions of the bulk starting material, experiment wire, and the total sample, we were able to quantify the mass of Fe lost and the associated Fe isotopic fractionation for both mechanisms of Fe loss occurring during an experimental run.

The incorporation of Fe into Re wire during the experiment induced some Fe isotopic fractionation, with the wire having a lighter iron isotopic composition than the total sample (Table 5, Fig. 5). Roskosz et al. (2006) demonstrated that experimental iron loss to Pt wires fractionates iron isotopes. In that study, kinetic fractionation of Fe isotopes produced an isotopically light Pt wire (relative to the experimental sample) in short duration experiments. In longer duration experiments, Fe isotopes equilibrated between the Pt wire and experimental charge producing an isotopically heavier Pt wire, which presumably represented the equilibrium partitioning of stable Fe isotopes between Pt and melt. Similar to the Pt wire results of Roskosz et al. (2006), the Re wires from our experiments are isotopically lighter than the experimental samples. This is most likely associated with diffusive transport of iron, as it is well-documented in a variety of systems that light isotopes diffuse faster than heavier ones (e.g., Richter et al., 2009; Van Orman and Krawczynski, 2015), resulting in light isotope enrichment in the reservoir that experiences net Fe gain (i.e., the Re wire) relative to the source (i.e., the silicate melt). Owing to this kinetic fractionation, iron isotopes are more fractionated between the Re wire and total sample in the experiments that experienced less iron loss ($fO_2 = IW+2$). That is, as more Fe diffuses into the Re wire, the fractionation between the wire and the sample

Table 5
Iron isotopic compositions. Reported values are the weighted averages and weighted errors (95% confidence interval) of multiple measurements.

Sample	Starting Composition	fO_2	Starting Material				Experiment Wire					Total Sample				Glass				Olivine			
			$\delta^{56}Fe$	2σ	$\delta^{57}Fe$	2σ	ug Fe	$\delta^{56}Fe$	2σ	$\delta^{57}Fe$	2σ	$\delta^{56}Fe$	2σ	$\delta^{57}Fe$	2σ	$\delta^{56}Fe$	2σ	$\delta^{57}Fe$	2σ	$\delta^{56}Fe$	2σ	$\delta^{57}Fe$	2σ
H056	Apollo 14 VLT (#029)	IW−1	0.26	0.04	0.38	0.06	434	0.13	0.04	0.37	0.06	0.65	0.04	1.01	0.06	0.60	0.04	0.93	0.06	0.60	0.04	0.96	0.06
H043	Apollo 14 Black (#011)	IW−1	0.06	0.02	0.08	0.05	924	0.06	0.03	0.08	0.07	0.28	0.04	0.46	0.06	0.27	0.03	0.43	0.07	0.28	0.03	0.46	0.07
H055	Apollo 14 Black (#028)	IW−1	0.32	0.04	0.44	0.06	722	0.42	0.04	0.67	0.06	0.57	0.04	0.89	0.06	0.54	0.04	0.88	0.06	0.54	0.04	1.04	0.06
H030	Apollo 14 VLT (#010)	IW+2	0.00	0.03	0.01	0.05	39	−0.53	0.05	−0.80	0.08	0.13	0.04	0.18	0.07	0.11	0.03	0.16	0.04	0.12	0.03	0.19	0.04
J012	Apollo 14 Black (#011)	IW+2	0.06	0.02	0.08	0.05	42	−0.37	0.05	−0.56	0.08	0.08	0.03	0.11	0.05	0.11	0.02	0.15	0.04	0.10	0.03	0.15	0.05

For N measurements and i = 1,... N, the weighted averages and weighted errors are calculated from the iron isotope composition and standard deviation on each measurement (i) using the following equations:

$w_i = 1/(\sigma_i^2)$, $\sigma_{average} = \frac{1}{\sqrt{(\sum w_i)}}$, $\delta^{56}Fe_{average} = \left(\sum(w_i\delta^{56}Fe_i)\right)/(\sum w_i)$.

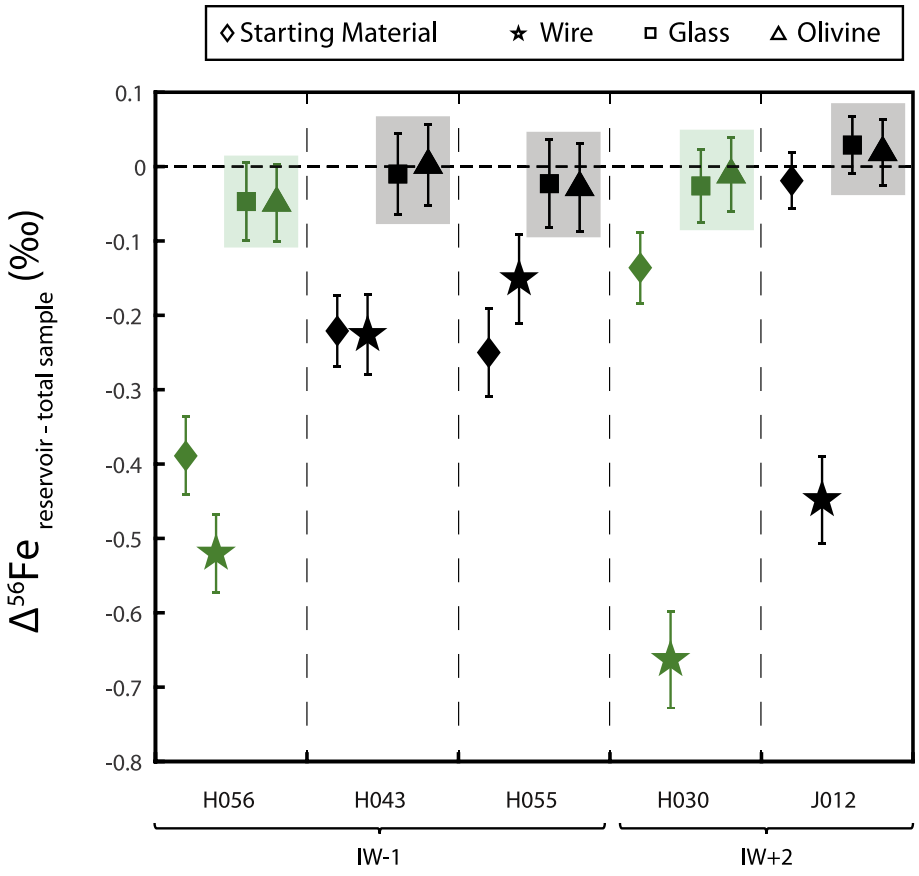

Fig. 5. Iron isotopic compositions for each experiment part from Table 5 reported as $\Delta^{56}Fe_{part\ -\ total\ sample}$ ($\delta^{56}Fe_{part} - \delta^{56}Fe_{total\ sample}$). Error bars represent 95% confidence interval. Green symbols indicate a synthetic green glass starting composition, and black symbols indicate a synthetic black glass starting composition. Olivine and glass pairs from a given experiment are highlighted.

decreases. Only one sample (H055) has a Re wire iron isotopic composition that is heavier than the iron isotopic composition of the bulk starting material, however the wire is still isotopically lighter than the glass. Owing to the presence of a thin glass coating on the H055 wire, it is possible that a minor amount of experimental glass was dissolved along with the wire during preparation for iron isotope measurement. This would result in a measured iron isotopic composition for the wire that is heavier than the iron isotopic composition of the wire without glass.

Although loss of Fe to the Re wire fractionates Fe isotopes and produces a heavier Fe isotopic composition for the total sample relative to the bulk starting material, the total amount of Fe incorporated into the wire cannot account for the magnitude of Fe isotopic fractionation between the two, nor the bulk Fe loss. Similar to Fe loss to the Re wire, evaporative Fe loss would preferentially deplete the experiments in lighter Fe isotopes, resulting in greater $\delta^{56}Fe$ for the olivine, glass, and total sample compared to the bulk starting material.

To assess the extent of both evaporative Fe loss and Fe loss to the Re wire, we calculated an isotopic mass balance of the measured experiment parts (starting material, wire, and total sample) and, by difference, the Fe that evaporated during the experiment. For example, using the isotopic measurements (Table 5) for each part of experiment H056 we can estimate a $\delta^{56}Fe$ for the Fe lost by evaporation:

$$\delta^{56}Fe_{starting\ \ material} = \sum_{i} \left(X^{i}_{Fe} \times \delta^{56}Fe_{i}\right) \quad (3)$$

where i denotes a reservoir of the experiment (wire, total sample, gas), where X_{Fe} represents the mass fraction of the initial Fe present in each reservoir, $\delta^{56}Fe_{starting\ material}$, $\delta^{56}Fe_{total\ sample}$, $\delta^{56}Fe_{wire}$ are measured values, and $\delta^{56}Fe_{gas}$, X^{wire}_{Fe}, $X^{total\ sample}_{Fe}$, X^{gas}_{Fe} can then be calculated from mass balance constraints (results presented in Fig. 6). $X^{total\ sample}_{Fe}$ is equivalent to one minus the percent total Fe loss estimated from mass balance of the measured phases and the experimental starting composition (Krawczynski and Olive, 2011). For H056, which experienced 18% total Fe loss, $X^{total\ \ sample}_{Fe} = 0.82$ (Fig. 6b). X^{wire}_{Fe} is calculated using the ICP-MS Fe concentration measurement of the dissolved wire (μg, Table 5) and the estimated mass of Fe in the starting material (75 mg pellet, wt.% FeO for starting composition, Table 1). For H056, $X^{wire}_{Fe} = 0.04$. Following this, X^{gas}_{Fe} can be calculated assuming $X^{total\ sample}_{Fe} + X^{wire}_{Fe} + X^{gas}_{Fe} = 1$. Thus, for H056, $X^{gas}_{Fe} = 0.14$. From this calculation, we conclude that 14% of the initial Fe in the starting material was lost by evaporation during the experiment.

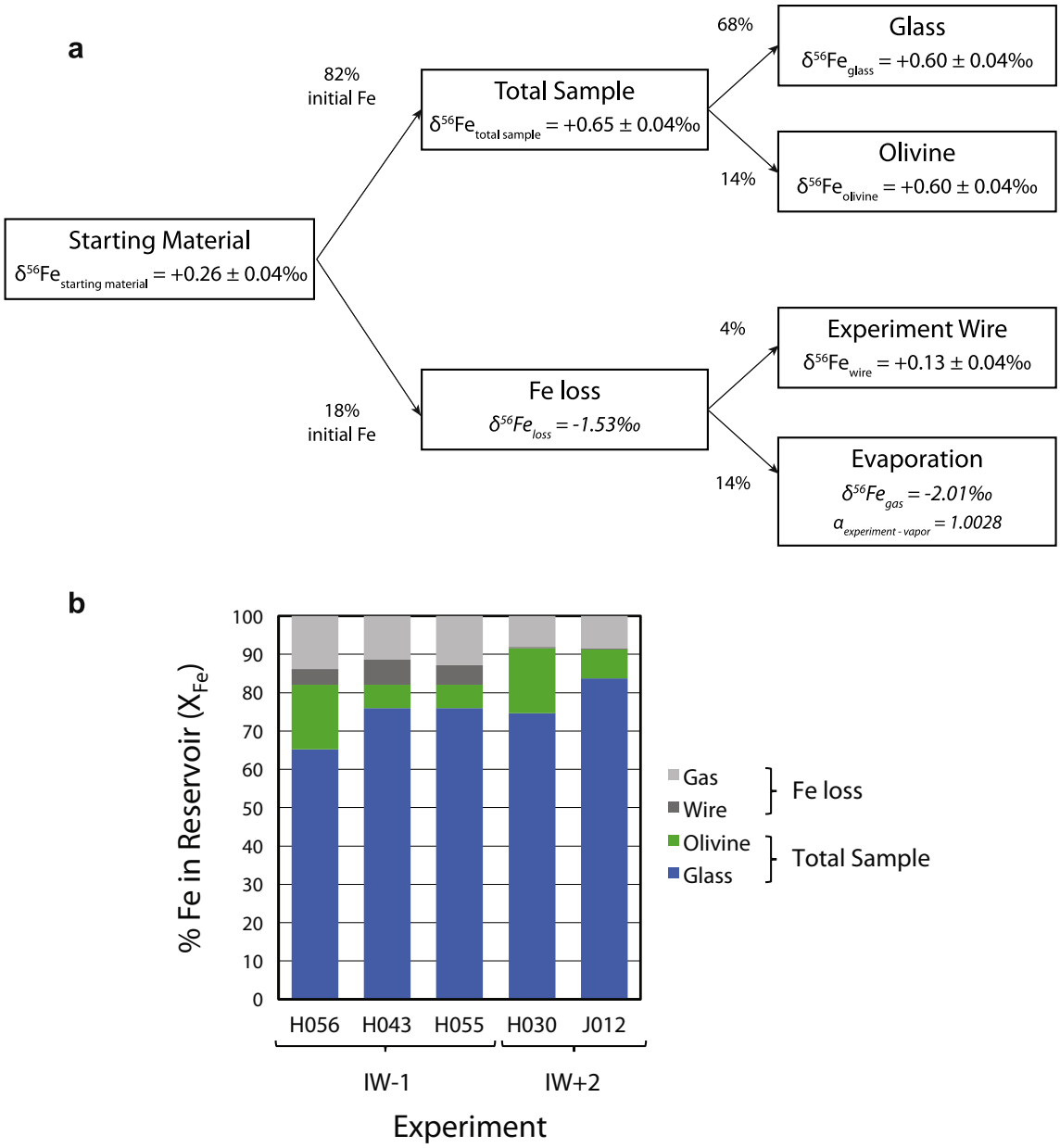

Fig. 6. (a) A schematic diagram illustrating the Fe mass and isotope distributions detailed in Section 4.1 for experiment H056. The labeled percent values at each branch represent the percent of the initial Fe attributed to a given experiment reservoir. Measured iron isotopic compositions of each experiment reservoir are mass balanced to explain the effect of Fe loss on the iron isotopic composition of the total sample. Iron isotopic compositions and fractionations in italics indicate calculated (not measured) values. Percent initial Fe for olivine and glass separates is calculated using the olivine and glass proportions given in Table 2 (83% glass, 17% olivine for H056) and the calculated percent initial Fe for the total sample ($X_{Fe}^{\text{total sample}} = 1 - X_{Fe}^{\text{loss}}$). A similar calculation was performed for each experiment using the measured iron isotopic compositions for all the experiment reservoirs (starting material, olivine, glass, total sample, experiment wire). (b) A stacked bar graph indicating the X_{Fe} calculated for each Fe reservoir for each experiment. The bracketed labels below the experiment names indicate the oxygen fugacity of the experiment (IW−1 or IW+2). Additionally, the legend identifies which reservoirs constitute Fe loss (wire, gas) and "total sample" Fe (olivine, glass).

The last unknown of Eq. (3) is the "iron isotopic composition" of the Fe lost through evaporation ($\delta^{56}Fe_{gas}$), or rather the net isotopic fractionation that resulted from the evaporation. To estimate the evaporative fractionation, we solve Eq. (3) for $\delta^{56}Fe_{gas}$ using the X_{Fe} values calculated above (Fig. 6b) and the measured $\delta^{56}Fe$ values for the experiment parts (Table 5). For H056, the resulting isotopic composition associated with the evaporated gas is $\delta^{56}Fe_{gas} = -2.01‰$, and the bulk isotopic fractionation factor is $\alpha_{\text{experiment-vapor}} = 1.0028$. Our estimates of the evaporative isotopic fractionation based on the mass balance of our measured experimental run products (bulk $\alpha_{\text{experiment-vapor}}$) range from 1.0002 to 1.0028, with the smallest fractionation between experiment and vapor

(1.0002) existing for experiment J012, the high-Ti (black glass) composition conducted at IW+2. The experiment-vapor fractionation in our gas-mixing furnace experiments is smaller than that in a vacuum furnace because the Fe vapor pressure is higher, which dampens the isotopic fractionation (Richter et al., 2002, 2007, 2009; Richter, 2004; Dauphas and Rouxel, 2006; Dauphas et al., 2015). Most likely, the evaporative Fe loss proceeded through a Rayleigh distillation. Using the $\alpha_{\text{experiment-vapor}}$ calculated for each experiment, we have modeled the change in the iron isotopic composition of the experimental sample as iron is lost by evaporation (Fig. 7).

For experiments conducted at $fO_2 = \text{IW}-1$, on average 5% of the Fe starting material was lost to the Re wire (average $X_{Fe}^{wire} = 0.05$), while this value is negligible at IW+2 (Fig. 6b). Additionally, 13% of the Fe starting material was lost via evaporation at IW−1 (average $X_{Fe}^{gas} = 0.13$) and 8% of the starting material Fe was lost by evaporation at IW+2 (average $X_{Fe}^{gas} = 0.08$). In one-atmosphere gas-mixing furnace experiments, Fe loss has generally been considered as loss to the container (e.g., Re or Pt wire), while volatile element loss (e.g., Na, K) has been attributed to vaporization (Corrigan and Gibb, 1979; Donaldson and Gibb, 1979; Grove, 1981; Borisov and Jones, 1999). Our results indicate that at IW−1, ~75% of the estimated Fe loss occurred via evaporation, and only 25% of the Fe loss can be attributed through loss to the Re wire. At IW+2, the estimated Fe loss is due to ~95% evaporative loss and ~5% loss to the Re wire.

To further assess the potential for evaporative isotopic fractionation at our experimental run conditions, we have calculated the evaporative flux of Fe (J_{Fe}) from the sample using the Hertz-Knudsen equation:

$$J_{Fe} = \frac{\alpha_{Fe}\left(P_{Fe}^{v} - P_{Fe}^{a}\right)}{\sqrt{2\pi M_{Fe} RT}} \quad (4)$$

in which J is the evaporative flux in moles cm^{-2} s^{-1}, α is the evaporation coefficient, M is molecular weight, P^v is equilibrium vapor pressure for the element considered, P^a is the ambient pressure for the element considered, R is the universal gas constant (J mol^{-1} K^{-1}), and T is temperature (K). Following the methods outlined in Fedkin et al. (2006), we calculated the equilibrium vapor pressure of Fe assuming both Fe and FeO species exist in the gas, and the only contribution of Fe to the furnace gas atmosphere is from the experimental sample:

$$P_{Fe}^{v} = P_{Fe}^{sample} = P_{FeO} + P_{Fe} \quad (5)$$

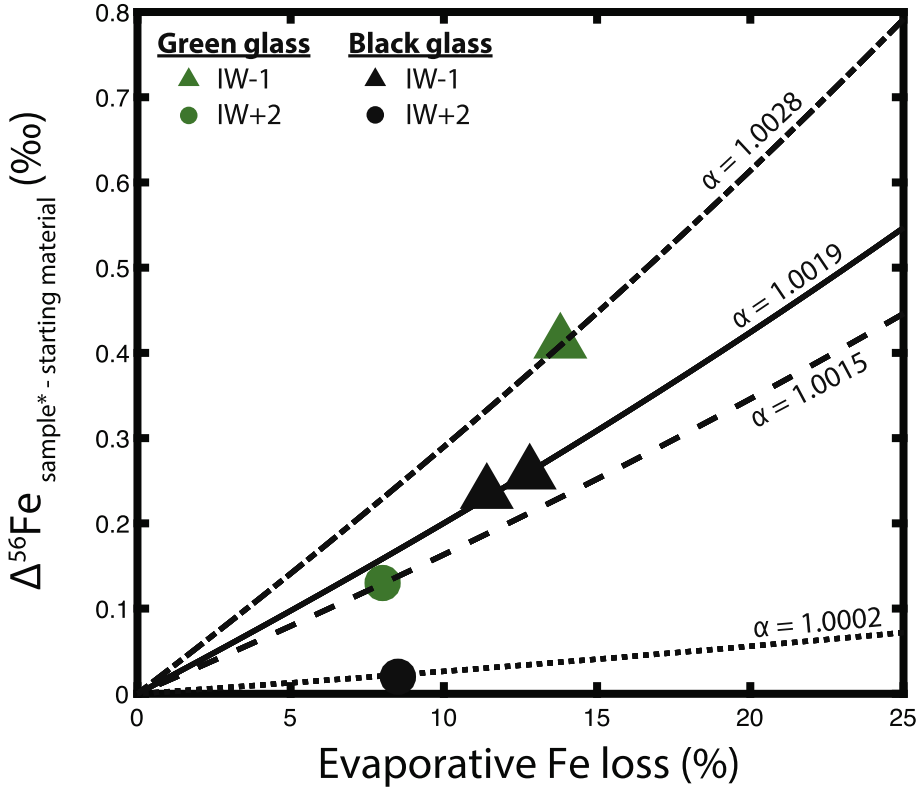

Fig. 7. The iron isotopic evolution of an experimental sample as evaporative Fe loss proceeds through Rayleigh distillation, as calculated using $\alpha_{\text{experiment-vapor}}$ for each experiment. The iron isotopic composition is reported as $\Delta^{56}Fe_{\text{sample*} - \text{starting material}}$ ($\delta^{56}Fe_{\text{sample*}} - \delta^{56}Fe_{\text{starting material}}$) using $\delta^{56}Fe_{\text{starting material}}$ from Table 5. $\delta^{56}Fe_{\text{sample*}}$ represents the iron isotopic composition of the "total sample" after accounting for the iron isotopic fractionation associated with Fe loss to the Re wire (Section 4.1, Fig. 6). This correction was performed to isolate the effect of evaporation on the heavy iron isotopic enrichment that occurs during the experiment, however both losses (to wire, to vapor) would occur simultaneously throughout the experiment. Green symbols indicate a synthetic green glass starting composition, and black symbols indicate a synthetic black glass starting composition. The shape of the symbols reflects the fO_2 of each experiment as indicated in the legend. Each modeled line is labeled with the corresponding $\alpha_{\text{experiment-vapor}}$ used in the Rayleigh distillation equation.

The partial pressures of the gases evaporated from the molten experimental sample are then calculated from the volatilization reactions:

$$FeO_{(l)} \rightarrow FeO_{(g)} \quad (6)$$

$$FeO_{(l)} \rightarrow Fe_{(g)} + \frac{1}{2}O_{2\,(g)} \quad (7)$$

The equilibrium constants, k, for reactions (6) and (7) are constructed from the thermodynamic data in the JANAF tables (Chase, 1996) and used to calculate the equilibrium vapor pressure of Fe:

$$P_{Fe}^{sample} = k_6 a_{FeO} + \frac{k_7 a_{FeO}}{\sqrt{fO_2}} \quad (8)$$

where a_{FeO} is the activity of FeO in the molten experimental sample, and fO_2 is the oxygen fugacity of the experiment. We used the rhyolite-MELTS code (Ghiorso and Sack, 1995; Asimow and Ghiorso, 1998; Gualda et al., 2012) to calculate the activity of FeO in the silicate liquid for each experimental starting composition at the experimental temperature and oxygen fugacity. Using Eq. (8), we calculate P_{Fe}^{sample}, which is then used to calculate the evaporative flux, J_{Fe}, from Eq. (4). Assuming the gas flow in our furnace is efficient in removing any Fe gas that is released into the furnace from the sample, we set the ambient vapor pressure of Fe (P^a) equal to 0. Then, the only unknown needed to solve for the evaporative flux (J_{Fe}) using Eq. (4) is the Fe evaporation coefficient (α_{Fe}). The evaporation coefficients we used in Eq. (4) to calculate evaporative Fe loss that matches the estimated evaporative Fe loss from our samples are $\alpha_{Fe} = 2.5 \times 10^{-3}$ at IW−1, and $\alpha_{Fe} = 6.3 \times 10^{-2}$ at IW+2 (see Supplementary Material for additional detail).

Through isotopic measurement and mass balance calculations of our experiments, we have demonstrated that isotopic fractionation during evaporation and loss to the experimental container are essential considerations for experimental studies of isotope partitioning. Despite this open system behavior, the olivine and glass phases were always in equilibrium, as diffusion in the melt is fast (at 1265 °C, anhydrous basaltic melt $D_{Fe} \sim 10^{-11}$ m^2/s; Zhang et al., 2010), and 10–50 μm diameter olivine grains would diffusively equilibrate at the experimental run temperature and duration. For example, at experimental conditions of 1265 °C and IW+2, a 50 μm olivine grain would equilibrate with respect to Fe and Mg in approximately 50 h (McDougall and Harrison, 1999; Dohmen and Chakraborty, 2007). The olivine and glass separates showed deviation from the starting material, but had identical isotopic composition to that of the "total sample" which diffusively maintained equilibrium. Thus, the measured Fe isotopic compositions of the olivine and glass can accurately be compared to interpret the olivine-melt Fe isotopic fractionation during olivine crystallization.

4.2. Factors controlling iron isotopic fractionation on the Moon

We have applied our results to test whether the lunar iron isotope "dichotomy" observed between the high- and low-Ti basalts can be explained by olivine crystallization or melt titanium content.

From our complementary NRIXS and olivine crystallization experiments, we have concluded that any equilibrium fractionation of iron isotopes between olivine and melt at lunar-like oxygen fugacities is not resolvable within analytical uncertainties. Olivine-melt Fe isotopic fractionation factors for the lunar volcanic glasses were determined from our measured force constants on the glass suite and the olivine NRIXS results from Dauphas et al. (2014) (Fig. 8). Our result from the MC-ICPMS olivine crystallization study is consistent with the Fe isotopic fractionation factors predicted by the NRIXS measurements on olivine (Dauphas et al., 2014) and the suite of lunar volcanic glasses (this study), in that there is not a resolvable iron isotopic fractionation. Some major element variations in lunar mare basalts can be attributed to differences in source compositions having experienced varying degrees of olivine fractionation (Shearer et al., 2006, and references therein). Additionally, extensive crystallization of the lunar magma ocean involving significant fractionation of olivine has been previously hypothesized as a mechanism for generating the isotopically heavy source regions for the high-Ti basalts (Wang et al., 2015). However, because olivine does not fractionate iron isotopes to a measureable extent, varying degrees of equilibrium olivine crystallization can be eliminated as a potential mechanism for generating the mare basalt iron isotope dichotomy. The fractionation of phases other than olivine, such as clinopyroxene and ilmenite, are likely more important in interpreting both the major element and isotopic compositions of the lunar mare basalt suites.

Both of our experimental approaches indicate that the difference in melt titanium content between low-Ti and high-Ti mare basalts cannot explain the observed iron isotope dichotomy. Partitioning of Fe into olivine has been shown to be a function of Ti content (Longhi et al., 1978; Xirouchakis et al., 2001; Krawczynski and Grove, 2012). Titanium influences the coordination environment of Fe^{2+} in silicate melt by forming Fe-Ti complexes, and as a result, Fe is preferentially incorporated into the melt relative to olivine (Krawczynski and Grove, 2012). However Fe isotope partitioning does not appear to correlate with melt titanium content, as demonstrated by our NRIXS force constant measurements (Table 4, Fig. 4) and our olivine crystallization experiments from both the low-Ti and high-Ti glass compositions. Within the investigated range of titanium content, the average coordination number of Fe^{2+}does not vary enough to influence the NRIXS force constants. Though the major element partitioning of Fe into olivine is affected by Fe^{2+}-Ti complexes in silicate melt, we conclude that the isotopic partitioning of Fe is not affected by melt titanium content. In contrast, Dauphas et al. (2014) demonstrated that melt compositional parameters such as silica content and the redox state of iron (i.e., Fe^{3+} content) influence the Fe bonding structure, and consequently, the iron isotopic composition, in a suite of terrestrial volcanic glass compositions ranging from basalt to rhyolite.

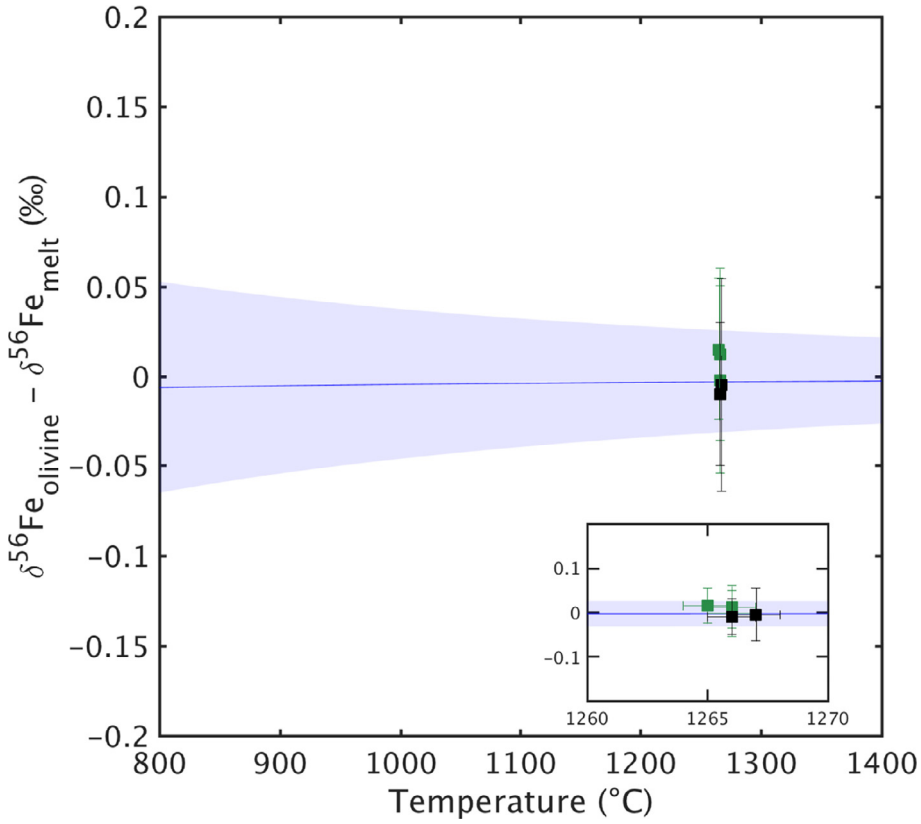

Fig. 8. Equilibrium mineral-melt fractionation of iron isotopes for olivine plotted as a function of temperature. The blue line represents the difference between the average beta factor calculated from the NRIXS mean force constants for our synthetic lunar glasses and the beta factor for olivine (Fo_{82}) from Dauphas et al. (2014). The blue shading represents the error associated with the calculated beta factors. The difference between the iron isotopic compositions of olivine and glass separates in each crystallization experiment (Table 5) are plotted with the associated measurement errors (95% confidence interval). Green symbols indicate a synthetic green glass starting composition, and black symbols indicate a synthetic black glass starting composition. The inset in the bottom right is the same data plotted in the main figure, with the x-axis expanded on the experiment run temperatures. There is no resolvable difference between olivine and the synthetic lunar glass suite under equilibrium conditions, as evidenced by our experimental results from both the NRIXS and ICPMS approaches.

4.3. Iron isotopic composition of lunar dunite 72415

Olivines from lunar dunite 72415 are considerably lighter than the mare basalts ($\delta^{56}Fe_{dunite} = -0.35 \pm 0.20$‰, Wang et al., 2015; Sossi and Moynier, 2017). These values, if representative of equilibrium fractionation from a parent melt isotopically similar to the mare basalts ($\delta^{56}Fe = 0$‰ to +0.2‰), differ from the predicted Fe isotopic fractionation of this study. The absence of resolvable equilibrium iron isotopic fractionation between olivine and lunar melts in our experiments supports a non-equilibrium model for generating the light iron isotopic composition of the lunar dunite.

As Fe begins to diffuse into olivine, the isotopes of Fe with lighter mass will be preferentially enriched, creating a "light" iron isotopic composition (Teng et al., 2008, 2011; Dauphas et al., 2010; Sio et al., 2013; Sio and Dauphas, 2017). The lunar dunite is highly magnesian (Fo_{84}–Fo_{89}, Dymek et al., 1975), and any Fe that diffuses into the olivine will greatly affect the mass balance of Fe isotopes in the dunite. Diffusive iron isotopic fractionation modeling that reproduces the observed Fe-Mg zoning profiles in lunar dunite olivine grains, can produce iron isotope signatures as low as $\delta^{56}Fe = -0.21$‰ and −0.3‰ (Wang et al. 2015). Further, kinetic isotopic fractionation models of Fe-Mg interdiffusion and olivine crystallization (Teng et al., 2008, 2011; Sio et al., 2013; Oeser et al., 2015; Collinet et al., 2017; Sio and Dauphas, 2017) reproduce isotopic fractionations as large as 1‰ observed in olivine grains.

Models of lunar dunite (72415–72418) petrogenesis detail the potential petrologic processes involved in generating a kinetic origin for the isotopically light dunite signature. Early petrologic investigations of the lunar dunite identified it as an early lunar magma ocean cumulate (e.g., Dymek et al., 1975). In contrast, Ryder (1992) concluded that the lunar dunite crystallized at shallow depths less than 1 km. The early lunar magma ocean cumulate hypothesis was invoked by Wang et al. (2015) to explain the isotopically light iron isotopic compositions of the dunite. If the lunar dunite is an early lunar magma ocean cumulate, then, assuming equilibrium conditions, the composition from which the dunite is crystallizing must already be isotopically light; $\delta^{56}Fe = -0.35 \pm 0.20$‰.

One way an isotopically light dunite source composition could potentially be generated is by an early core formation and metal-silicate partitioning. Experimental and ana-

lytical studies of metal-silicate iron isotope partitioning have suggested that metal is isotopically heavier ($\Delta^{56}Fe_{metal\text{-}silicate} \approx +0.1‰$) than coexisting silicate (Poitrasson et al., 2005; Shahar et al., 2015; Elardo and Shahar, 2017). However, a number of investigations (e.g., Schuessler et al., 2007; Poitrasson et al., 2009; Hin et al., 2012; Shahar et al., 2016; Liu et al., 2017) have concluded that no significant iron isotopic fractionation occurs between metal and silicate in equilibrium. The disagreement results from the significant differences in starting compositions, phases, capsule materials, and experimental conditions between studies. Assuming an equilibrium iron isotopic fractionation did exist between metal and silicate, if the dunite source were once deep enough to be in isotopic equilibrium with the lunar core, it would have a relatively light iron isotopic composition. However, the estimates for the bulk mantle iron isotopic composition of the Moon after core formation (e.g., minimum $\delta^{56}Fe = -0.15‰$; Elardo and Shahar, 2017), still cannot explain the magnitude of light iron isotopic compositions measured in the lunar dunite by equilibrium metal-silicate fractionation alone.

Another alternative method of generating isotopically light olivine in the lunar dunite is partial melting. Iron isotope studies of terrestrial peridotites, which are the residues of partial melting and depletion, show a correlation between iron isotopic compositions and depletion, becoming lighter at higher extents of partial melting (Williams et al., 2005, 2009; Weyer and Ionov, 2007; Williams and Bizimis, 2014). It is possible that the iron isotopic composition of the lunar dunite is a result of partial melting, however the existing models of lunar dunite petrogenesis (i.e., Dymek et al., 1975; Ryder, 1992; Shearer et al., 2015) identify the dunite as being of cumulate origin, not an ultra-depleted residue of partial melting.

Considering the potential models for lunar dunite petrogenesis, kinetic fractionation via Fe-Mg interdiffusion seems likely to have occurred, and this mechanism could easily explain the light Fe isotopic compositions measured in the lunar dunite olivines. Regardless of whether the lunar dunite is a deep magma ocean cumulate (Dymek et al., 1975) or shallow cumulate (Ryder, 1992; Shearer et al., 2015), the Mg-rich nature of the dunite ensures it would have interacted with a higher Fe/Mg melt before and/or during its ascent to the lunar surface/sub-surface. In this way, iron diffusion into the dunite is a plausible occurrence during every proposed model of dunite formation. Iron diffusion into the Fe-poor olivine of the lunar dunite would decrease the $\delta^{56}Fe$ composition, producing the negative $\delta^{56}Fe$ values measured by both Wang et al. (2015) and Sossi and Moynier (2017).

4.4. Considerations for high-temperature iron isotopic fractionation on Earth and Mars

The results of our olivine crystallization experiments indicate that the absence of a measureable equilibrium iron isotopic fractionation between olivine and melt is robust over $fO_2 = IW-1$ to IW+2 in both the low-Ti (green glass) and high-Ti (black glass) compositions. Thus, we can apply our results for the synthetic lunar glass compositions to olivine-bearing systems on Earth and Mars with a similar range in oxygen fugacity, keeping in mind that there could be melt compositional controls in addition to that of TiO_2 determined in this work.

Estimations for the oxygen fugacity of Earth's upper mantle from spinel peridotites lie within QFM ± 2 (IW+1.5 to IW+5.5 at magmatic temperatures), with select abyssal peridotites and peridotite massifs extending to QFM-3 (~IW+0.5) (Frost and McCammon, 2008, and references therein). Garnet peridotites are more reducing than spinel peridotites, with the majority of fO_2 estimations falling between IW−1 and IW+2 (Frost and McCammon, 2008). Additionally, the oxygen fugacity of martian basalts is estimated to be QFM-3 to QFM-1 (~IW to IW+3) (Herd et al., 2002). Considering these estimates of magmatic oxygen fugacity, the IW−1 to IW+2 range of our experiments is relevant to garnet peridotites, as well as the most reduced spinel peridotites and martian basalts.

Iron isotopic compositions of terrestrial peridotites are $\delta^{56}Fe = -0.1‰$ to $+0.15‰$ (Dauphas et al., 2017). The range of peridotite iron isotopic compositions are considered to be a result of melt extraction based on the correlation between iron isotopic composition and depletion, with iron isotopic compositions of residues becoming lighter at higher extents of partial melting (Williams et al., 2005, 2009; Weyer and Ionov, 2007; Williams and Bizimis, 2014). Alternatively, the heavy isotopic enrichment in the melt relative to the residue may be a result of Fe^{3+} in the melt (Dauphas et al., 2009a, 2014). For instance, the difference between the iron isotopic compositions of spinel and garnet peridotites has been attributed to the contrasting behavior of Fe^{3+} during melting (Williams et al., 2005). Experimental determinations of mineral-melt iron isotopic fractionations for additional minerals (i.e., pyroxene, spinel) are needed in order to fully model the evolution of iron isotopic compositions during partial melting, as there exists experimental evidence for equilibrium iron isotopic fractionation between spinel and olivine (Shahar et al., 2008; Roskosz et al., 2015).

5. CONCLUSION

Olivine separates are often enriched in lighter iron isotopes relative to coexisting minerals and the bulk rock (e.g., terrestrial peridotites, Beard and Johnson (2004); Poitrasson et al. (2004); Williams et al. (2005); terrestrial basalts, Teng et al. (2008, 2011); Sio et al. (2013); lunar basalts, Poitrasson et al. (2004); Wang et al. (2012); Wang et al. (2015); martian basalts, Collinet et al. (2017)). Considering the olivine-melt fractionation results presented in this work, the only known mechanism capable of fractionating iron isotopes to a measureable degree is diffusive fractionation (Dauphas et al., 2010; Teng et al., 2011; Sio et al., 2013; Oeser et al., 2015; Sio and Dauphas, 2016; Collinet et al., 2017). Thus, the olivine grains enriched in light Fe isotopes in mafic rocks are not a result of primary igneous crystallization, but rather a diffusive fractionation, potentially

related to re-equilibration (Teng et al., 2011; Sio et al., 2013; Oeser et al., 2015) or simultaneous Fe diffusion and crystal growth (Sio and Dauphas, 2016; Collinet et al., 2017). A diffusive fractionation mechanism is further supported by existing isotopic disequilibrium between coexisting mineral pairs in peridotite samples (Beard and Johnson, 2004; Roskosz et al., 2015). This disequilibrium in peridotites has been hypothesized as a result of multiple phases of melt extraction, melt percolation, melt-rock reaction, or metasomatism (Beard and Johnson, 2004; Williams et al., 2005; Macris et al., 2015; Roskosz et al., 2015; Zhao et al., 2017). If the light iron isotopic compositions of terrestrial peridotites can conclusively be attributed to metasomatism, then the light iron isotopic composition of the lunar dunite (discussed in Section 4.3) may also be a result of metasomatism, as metasomatism has been invoked to explain chemical trends and petrographic textures observed in the lunar dunite (Shearer et al., 2015).

ACKNOWLEDGEMENTS

This work was supported by NASA grant NNX15AJ25G to MJK and ND, the McDonnell Center for the Space Sciences Roger B. Chaffee fellowship to KBP, and NSF (CSEDI EAR1502591 and Petrology and Geochemistry grant EAR1444951) and NASA (LARS NNX17AE86G, EW NNX17AE87G) grants to ND. The authors would like to thank Paul Carpenter for his assistance with electron microprobe analyses, Prof. Robert Dymek for helpful discussions concerning the petrology of lunar dunite 72415–72418, as well as Dr. Katharina Lodders for insight regarding the thermodynamics and kinetics of iron vaporization. Additionally, the authors thank Drs. Helen Williams, Catherine Macris, and Yongsheng He for providing thoughtful, constructive reviews of this manuscript, as well as Dr. Shichun Huang for additional comments and editorial handling.

APPENDIX A. SUPPLEMENTARY MATERIAL

Supplementary data associated with this article can be found, in the online version, at https://doi.org/10.1016/j.gca.2018.07.028.

REFERENCES

Asimow P. D. and Ghiorso M. S. (1998) Algorithmic modifications extending MELTS to calculate subsolidus phase relations. *Am. Mineral.* **83**, 1127–1131.

Beard B. L. and Johnson C. M. (2004) Inter-mineral Fe isotope variations in mantle-derived rocks and implications for the Fe geochemical cycle. *Geochim. Cosmochim. Acta* **68**, 4727–4743.

Borisov A. and Jones J. H. (1999) An evaluation of Re, as an alternative to Pt, for the 1 bar loop technique: an experimental study at 1400 °C. *Am. Mineral.* **84**, 1528–1534.

Chase M. W. (1996) NIST-JANAF thermochemical tables for the bromine oxides. *J. Phys. Chem. Ref. Data* **25**, 1069.

Collinet M., Charlier B., Namur O., Oeser M., Médard E. and Weyer S. (2017) Crystallization history of enriched shergottites from Fe and Mg isotope fractionation in olivine megacrysts. *Geochim. Cosmochim. Acta* **207**, 277–297.

Corrigan G. and Gibb F. G. F. (1979) The loss of Fe and Na from a basaltic melt during experiments using wire-loop method. *Mineral. Mag.* **43**, 121–126.

Craddock P. R. and Dauphas N. (2011) Iron isotopic compositions of geologic reference materials and chondrites. *Geostand. Geoanal. Res.* **35**, 101–123.

Craddock P. R., Dauphas N. and Clayton R. N. (2010) Mineralogical control on iron isotopic fractionation during lunar differentiation and magmatism. *41st Lunar and Planetary Science Conference, Houston, TX*, p. 1230.

Dauphas N. (2007) Diffusion-driven kinetic isotope effect of Fe and Ni during formation of Widmanstätten pattern. *Meteorit. Planet. Sci.*, 1597–1613.

Dauphas N., Craddock P. R., Asimow P. D., Bennett V. C., Nutman A. P. and Ohnenstetter D. (2009a) Iron isotopes may reveal the redox conditions of mantle melting from Archean to Present. *Earth Planet. Sci. Lett.* **288**, 255–267.

Dauphas N., Janney P. E., Mendybaev R. A., Wadhwa M., Richter F. M., Davis A. M., van Zuilen M., Hines R. and Foley C. N. (2004) Chromatographic separation and multicollection-ICPMS analysis of iron. Investigating mass-dependent and -independent isotope effects. *Anal. Chem.* **76**, 5855–5863.

Dauphas N., John S. G. and Rouxel O. (2017) Iron isotope systematics. *Rev. Mineral. Geochem.* **82**, 415–510.

Dauphas N., Poitrasson F., Burkhardt C., Kobayashi H. and Kurosawa K. (2015) Planetary and meteoritic Mg/Si and δ30Si variations inherited from solar nebular chemistry. *Earth Planet. Sci. Lett.*, 236–248.

Dauphas N., Pourmand A. and Teng F.-Z. (2009b) Routine isotopic analysis of iron by HR-MC-ICPMS: how precise and how accurate?. *Chem. Geol.* **267** 175–184.

Dauphas N., Roskosz M., Alp E. E., Golden D. C., Sio C. K., Tissot F. L. H., Hu M. Y., Zhao J., Gao L. and Morris R. V. (2012) A *general moment* NRIXS approach to the determination of equilibrium Fe isotopic fractionation factors: Application to goethite and jarosite. *Geochim. Cosmochim. Acta* **94**, 254–275.

Dauphas N., Roskosz M., Alp E. E., Neuville D. R., Hu M. Y., Sio C. K., Tissot F. L. H., Zhao J., Tissandier L., Médard E. and Cordier C. (2014) Magma redox and structural controls on iron isotope variations in Earth's mantle and crust. *Earth Planet. Sci. Lett.* **398**, 127–140.

Dauphas N. and Rouxel O. (2006) Mass spectrometry and natural variations of iron isotopes. *Mass Spectrom. Rev.* **25**, 515–550.

Dauphas N., Teng F. Z. and Arndt N. T. (2010) Magnesium and iron isotope in 2.7 Ga Alexo komatiites: mantle signatures, no evidence for Soret diffusion, and identification of diffusive transport in zoned olivine. *Geochim. Cosmochim. Acta* **74**, 3274–3291.

Day J. M. D., Qiu L., Ash R. D., McDonough W. F., Teng F.-Z., Rudnick R. L. and Taylor L. A. (2016) Evidence for high-temperature fractionation of lithium isotopes during differentiation of the Moon. *Meteorit. Planet. Sci.* **51**, 1046–1062.

Delano J. W. (1986) Pristine lunar glasses: criteria, data, and implications. *J. Geophys. Res.* **91**, D201–D213.

Dohmen R. and Chakraborty S. (2007) Fe-Mg diffusion in olivine II: point defect chemistry, change of diffusion mechanisms and a model for calculation of diffusion coefficients in natural olivine. *Phys. Chem. Miner.* **34**, 409–430.

Donaldson C. H. and Gibb F. G. F. (1979) Changes in sample composition during experiments using 'wire-loop' technique. *Mineral. Mag.* **43**, 115–119.

Donovan J. J., Singer J. W. and Armstrong J. T. (2016) A new EPMA method for fast trace element analysis in simple matrices. *Am. Mineral.* **101**, 1839–1853.

Dymek R. F., Albee A. L. and Chodos A. A. (1975) Comparative petrology of lunar cumulate rocks of possible primary origin: Dunite 72415, troctolite 76535, norite 78235, and anorthosite 62237. In *Proceedings of the 6th Lunar Science Conference*, pp. 301–341.

Elardo S. M. and Shahar A. (2017) Non-chondritic iron isotope ratios in planetary mantles as a result of core formation. *Nat. Geosci.* **10**, 317–321.

Fedkin A. V., Grossman L. and Ghiorso M. S. (2006) Vapor pressures and evaporation coefficients for melts of ferromagnesian chondrule-like compositions. *Geochim. Cosmochim. Acta* **70**, 206–223.

Frost D. J. and McCammon C. A. (2008) The redox state of earth's mantle. *Annu. Rev. Earth Planet. Sci.* **36**, 389–420.

Ghiorso M. S. and Sack R. O. (1995) Chemical mass transfer in magmatic processes. IV. A revised and internally consistent thermodynamic model for the interpolation and extrapolation of liquid-solid equilibria in magmatic systems at elevated temperatures and pressures. *Contrib. Miner. Petrol.* **119**, 197–212.

Grove T. L. (1981) Use of FePt alloys to eliminate the iron loss problem in 1 atmosphere gas mixing experiments: theoretical and practical considerations. *Contrib. Miner. Petrol.* **78**, 298–304.

Gualda G. A. R., Ghiorso M. S., Lemons R. V. and Carley T. L. (2012) Rhyolite-MELTS: A modified calibration of MELTS optimized for silica-rich, fluid-bearing magmatic systems. *J. Petrol.* **53**, 875–890.

Herd C. D. K., Borg L. E., Jones J. H. and Papike J. J. (2002) Oxygen fugacity and geochemical variations in the martian basalts: Implications for martian basalt petrogenesis and the oxidation state of the upper mantle of Mars. *Geochim. Cosmochim. Acta* **66**, 2025–2036.

Hin R. C., Schmidt M. W. and Bourdon B. (2012) Experimental evidence for the absence of iron isotope fractionation between metal and silicate liquids at 1 GPa and 1250–1300 °C and its cosmochemical consequences. *Geochim. Cosmochim. Acta* **93**, 164–181.

Krawczynski M. J. and Grove T. L. (2012) Experimental investigation of the influence of oxygen fugacity on the source depths for high titanium lunar ultramafic magmas. *Geochim. Cosmochim. Acta* **79**, 1–19.

Krawczynski, M.J., Olive, J.L., 2011. A new fitting algorithm for petrological mass-balance problems. AGU Fall Meeting Abstracts, p. 2613.

Liu J., Dauphas N., Roskosz M., Hu M. Y., Yang H., Bi W., Zhao J., Alp E. E., Hu J. Y. and Lin J.-F. (2017) Iron isotopic fractionation between silicate mantle and metallic core at high pressure. *Nat. Commun.* **8**, 14377.

Liu Y., Spicuzza M. J., Craddock P. R., Day J. M. D., Valley J. W., Dauphas N. and Taylor L. A. (2010) Oxygen and iron isotope constraints on near-surface fractionation effects and the composition of lunar mare basalt source regions. *Geochim. Cosmochim. Acta* **74**, 6249–6262.

Longhi J., Walker D. and Hays J. F. (1978) The distribution of Fe and Mg between olivine and lunar basaltic liquids. *Geochim. Cosmochim. Acta* **42**, 1545–1558.

Macris C. A., Manning C. E. and Young E. D. (2015) Crystal chemical constraints on inter-mineral Fe isotope fractionation and implications for Fe isotope disequilibrium in San Carlos mantle xenoliths. *Geochim. Cosmochim. Acta* **154**, 168–185.

McDougall I. and Harrison T. M. (1999) *Geochronology and Thermochronology by the 40Ar/39Ar Method*, second ed. Oxford University Press, New York, NY.

Millet M. A., Dauphas N., Greber N. D., Burton K. W., Dale C. W., Debret B., Macpherson C. G., Nowell G. M. and Williams H. M. (2016) Titanium stable isotope investigation of magmatic processes on the Earth and Moon. *Earth Planet. Sci. Lett.* **449**, 197–205.

Mullen J. G. (1961) Isotope effect in intermetallic diffusion. *Phys. Rev.*, 1649–1658.

Oeser M., Dohmen R., Horn I., Schuth S. and Weyer S. (2015) Processes and time scales of magmatic evolution as revealed by Fe-Mg chemical and isotopic zoning in natural olivines. *Geochim. Cosmochim. Acta* **154**, 130–150.

Poitrasson F., Halliday A. N., Lee D.-C., Levasseur S. and Teutsch N. (2004) Iron isotope differences between Earth, Moon, Mars and Vesta as possible records of contrasted accretion mechanisms. *Earth Planet. Sci. Lett.* **223**, 253–266.

Poitrasson F., Levasseur S. and Teutsch N. (2005) Significance of iron isotope mineral fractionation in pallasites and iron meteorites for the core-mantle differentiation of terrestrial planets. *Earth Planet. Sci. Lett.* **234**, 151–164.

Poitrasson F., Roskosz M. and Corgne A. (2009) No iron isotope fractionation between molten alloys and silicate melt to 2000 °C and 7.7 GPa: experimental evidence and implications for planetary differentiation and accretion. *Earth Planet. Sci. Lett.* **278**, 376–385.

Polyakov V. B., Clayton R. N., Horita J. and Mineev S. D. (2007) Equilibrium iron isotope fractionation factors of minerals: reevaluation from the data of nuclear inelastic resonant X-ray scattering and Mössbauer spectroscopy. *Geochim. Cosmochim. Acta* **71**, 3833–3846.

Richter F. M. (2004) Timescales determining the degree of kinetic isotope fractionation by evaporation and condensation. *Geochim. Cosmochim. Acta* **68**, 4971–4992.

Richter F. M., Dauphas N. and Teng F.-Z. (2009) Non-traditional fractionation of non-traditional isotopes: evaporation, chemical diffusion and Soret diffusion. *Chem. Geol.* **258**, 92–103.

Richter F. M., Davis A. M., Ebel D. S. and Hashimoto A. (2002) Elemental and isotopic fractionation of Type B calcium-, aluminum-rich inclusions: experiments, theoretical considerations, and constraints on their thermal evolution. *Geochim. Cosmochim. Acta* **66**, 521–540.

Richter F. M., Janney P. E., Mendybaev R. A., Davis A. M. and Wadhwa M. (2007) Elemental and isotopic fractionation of Type B CAI-like liquids by evaporation. *Geochim. Cosmochim. Acta* **71**, 5544–5564.

Roskosz M., Luais B., Watson H. C., Toplis M. J., Alexander C. M. O. D. and Mysen B. O. (2006) Experimental quantification of the fractionation of Fe isotopes during metal segregation from a silicate melt. *Earth Planet. Sci. Lett.* **248**, 851–867.

Roskosz M., Sio C. K. I., Dauphas N., Wenli B., Tissot F. L. H., Hu M. Y., Zhao J. and Alp E. E. (2015) Spinel-olivine-pyroxene equilibrium iron isotopic fractionation and applications to natural peridotites. *Geochim. Cosmochim. Acta* **169**, 184–199.

Ryder G. (1992) Chemical variation and zoning of olivine in lunar dunite 72415: near-surface accumulation. In *Proceedings of Lunar and Planetary Science*, pp. 373–380.

Sato M. (1973) Oxygen fugacity values of Apollo 12, 14, and 15 lunary samples and reduced state of lunar magmas. In *Lunar and Planetary Science Conference Proceedings*, pp. 1061–1079.

Schuessler J. A., Schoenberg R., Behrens H. and von Blanckenburg F. (2007) The experimental calibration of the iron isotope fractionation factor between pyrrhotite and peralkaline rhyolitic melt. *Geochim. Cosmochim. Acta* **71**, 417–433.

Schuessler J. A., Schoenberg R. and Sigmarsson O. (2009) Iron and lithium isotope systematics of the Hekla volcano, Iceland – evidence for Fe isotope fractionation during magma differentiation. *Chem. Geol.* **258**, 78–91.

Sedaghatpour F., Teng F.-Z., Liu Y., Sears D. W. and Taylor L. A. (2013) Magnesium isotopic composition of the Moon. *Geochim. Cosmochim. Acta* **120**, 1–16.

Shahar A., Hillgren V. J., Horan M. F., Mesa-Garcia J., Kaufman L. A. and Mock T. D. (2015) Sulfur-controlled iron isotope

fractionation experiments of core formation in planetary bodies. *Geochim. Cosmochim. Acta* **150**, 253–264.
Shahar A., Schauble E. A., Caracas R., Gleason A. E., Reagan M. M., Xiao Y., Shu J. and Mao W. (2016) Pressure-dependent isotopic composition of iron alloys. *Science (New York, N.Y.)* **352**, 580–582.
Shahar A., Young E. D. and Manning C. E. (2008) Equilibrium high-temperature Fe isotope fractionation between fayalite and magnetite: an experimental calibration. *Earth Planet. Sci. Lett.* **268**, 330–338.
Shearer C. K., Elardo S. M., Petro N. E., Borg L. E. and McCubbin F. M. (2015) Origin of the lunar highlands Mg-suite: an integrate petrology, geochemistry, chronology, and remote sensing perspective. *Am. Mineral.* **100**, 294–325.
Shearer C. K., Hess P. C., Wieczorek M. A., Pritchard M. E., Parmentier E. M., Borg L. E., Longhi J., Elkins-Tanton L. T., Neal C. R., Antonenko I., Canup R. M., Halliday A. N., Grove T. L., Hager B. H., Lee D.-C. and Wiechert U. (2006) Thermal and magmatic evolution of the moon. *Rev. Mineral. Geochem.* **60**, 365–518.
Sio C. K. I. and Dauphas N. (2016) Thermal and crystallization histories of magmatic bodies by Monte Carlo inversion of Mg-Fe isotopic profiles in olivine. *Geology*.
Sio C. K. I. and Dauphas N. (2017) Thermal and crystallization histories of magmatic bodies by Monte Carlo inversion of Mg-Fe isotopic profiles in olivine. *Geology* **45**, 67–70.
Sio C. K. I., Dauphas N., Teng F.-Z., Chaussidon M., Helz R. T. and Roskosz M. (2013) Discerning crystal growth from diffusion profiles in zoned olivine by *in situ* Mg-Fe isotopic analyses. *Geochim. Cosmochim. Acta* **123**, 302–321.
Sossi P. A. and Moynier F. (2017) Chemical and isotopic kinship of iron in the Earth and Moon deduced from the lunar Mg-Suite. *Earth Planet. Sci. Lett.* **471**, 125–135.
Teng F.-Z., Dauphas N. and Helz R. T. (2008) Iron Isotope Fractionation During Magmatic Differentiation in Kilauea Iki Lava Lake. *Science (New York, N.Y.)* **320**, 1620–1622.
Teng F.-Z., Dauphas N., Helz R. T., Gao S. and Huang S. (2011) Diffusion-driven magnesium and iron isotope fractionation in Hawaiian olivine. *Earth Planet. Sci. Lett.* **308**, 317–324.
Teng, F.-Z., Dauphas, N., Watkins, J.M., 2017. Non-traditional stable isotopes.
Van Orman J. A. and Krawczynski M. J. (2015) Theoretical constraints on the isotope effect for diffusion in minerals. *Geochim. Cosmochim. Acta* **164**, 365–381.
Wang K. and Jacobsen S. B. (2016) Potassium isotopic evidence for a high-energy giant impact origin of the Moon. *Nature* **538**, 487–490.
Wang K., Jacobsen S. B., Sedaghatpour F., Chen H. and Korotev R. L. (2015) The earliest Lunar Magma Ocean differentiation recorded in Fe isotopes. *Earth Planet. Sci. Lett.* **430**, 202–208.
Wang K., Moynier F., Dauphas N., Barrat J.-A., Craddock P. R. and Sio C. K. (2012) Iron isotope fractionation in planetary crusts. *Geochim. Cosmochim. Acta* **89**, 31–45.
Weyer S., Anbar A. D., Brey G. P., Münker C., Mezger K. and Woodland A. B. (2005) Iron isotope fractionation during planetary differentiation. *Earth Planet. Sci. Lett.* **240**, 251–264.
Weyer S. and Ionov D. A. (2007) Partial melting and melt percolation: the message from Fe isotopes. *Earth Planet. Sci. Lett.* **259**, 119–133.
Wiesli R. A., Beard B. L., Taylor L. A. and Johnson C. M. (2003) Space weathering processes on airless bodies: Fe isotope fractionation in the lunar regolith. *Earth Planet. Sci. Lett.* **216**, 457–465.
Williams H. M. and Bizimis M. (2014) Iron isotope tracing of mantle heterogeneity within the source regions of oceanic basalts. *Earth Planet. Sci. Lett.* **404**, 396–407.
Williams H. M., Nielsen S. G., Renac C., Griffin W. L., O'Reilly S. Y., McCammon C. A., Pearson N., Viljoen F., Alt J. C. and Halliday A. N. (2009) Fractionation of oxygen and iron isotopes by partial melting processes: Implications for the interpretation of stable isotopes signatures in mafic rocks. *Earth Planet. Sci. Lett.* **283**, 156–166.
Williams H. M., Peslier A. H., McCammon C. A., Halliday A. N., Levasseur S., Teutsch N. and Burg J.-P. (2005) Systematic iron isotope variations in mantle rocks and minerals: The effects of partial melting and oxygen fugacity. *Earth Planet. Sci. Lett.* **235**, 435–452.
Xirouchakis D., Hirschmann M. M. and Simpson J. A. (2001) The effect of titanium on the silica content and on mineral-liquid partitioning of mantle-equilibrated melts. *Geochim. Cosmochim. Acta* **65**, 2201–2217.
Zhang Y., Ni H. and Chen Y. (2010) Diffusion in silicate melts. *Rev. Mineral. Geochem.* **72**, 311–408.
Zhao X., Zhang Z., Huang S., Liu Y., Li X. and Zhang H. (2017) Coupled extremely light Ca and Fe isotopes in peridotites. *Geochim. Cosmochim. Acta* **208**, 368–380.

Associate editor: Shichun Huang